Listvenite–lode association at the Barramiya gold mine, Eastern Desert, Egypt

Basem Zoheir [a,*], Bernd Lehmann [b]

[a] Department of Geology, Faculty of Science, Benha University, 13518 Benha, Egypt
[b] Mineral Resources, Technical University of Clausthal, 38678 Clausthal-Zellerfeld, Germany

ARTICLE INFO

ABSTRACT

Several occurrences of gold-bearing quartz veins are situated along the east–northeast-trending Barramiya–Um Salatit ophiolitic belt in the central Eastern Desert of Egypt. In the Barramiya mine, gold mineralization within carbonaceous, listvenized serpentinite and adjacent to post-tectonic granite stocks points toward a significant role of listvenitization in the ore genesis. The mineralization is related to quartz and quartz–carbonate lodes in silicified/carbonatized wallrocks. Ore minerals, disseminated in the quartz veins and adjacent wallrocks are mainly arsenopyrite, pyrite and trace amounts of chalcopyrite, sphalerite, tetrahedrite, pyrrhotite, galena, gersdorffite and gold. Partial to complete replacement of arsenopyrite by pyrite and/or marcasite is common. Other secondary phases include covellite and goethite. Native gold and gold–silver alloy occur as tiny grains along micro-fractures in the quartz veins. However, the bulk mineralization can be attributed to auriferous arsenopyrite and arsenic-bearing pyrite (with hundreds of ppms of refractory Au), as evident by electron microprobe and LA-ICP-MS analyses.

The mineralized quartz veins are characterized by abundant carbonic ($CO_2 \pm CH_4 \pm H_2O$) and aqueous-carbonic ($H_2O–NaCl–CO_2 \pm CH_4$) inclusions along intragranular trails, whereas aqueous inclusions ($H_2O–NaCl \pm CO_2$) are common in secondary sites. Based on the fluid inclusions data combined with thermometry of the auriferous arsenopyrite, the pressure–temperature conditions of the Barramiya gold mineralization range from 1.3 to 2.4 kbar at 325–370 °C, consistent with mesothermal conditions. Based on the measured $\delta^{34}S$ values of pyrite and arsenopyrite intimately associated with gold, the calculated $\delta^{34}S_{\Sigma s}$ values suggest that circulating magmatic, dilute aqueous-carbonic fluids leached gold and isotopically light sulfur from the ophiolitic sequence. As the ore fluids infiltrated into the sheared listvenite rocks, a sharp decrease in the fluid fO_2 via interaction with the carbonaceous wallrocks triggered gold deposition in structurally favorable sites.

© 2010 Elsevier B.V. All rights reserved.

1. Introduction

Listvenite is the product of intermediate-low temperature potassic metasomatism of mafic–ultramafic rocks (especially serpentinites), and is commonly located along regional shear zones (Halls and Zhao, 1995). With the influx of K-bearing hydrothermal fluids in tectonic structures, primary ferromagnesian silicates in the host rocks are replaced by Mg–Fe (–Ca) carbonates. Silica is released to form quartz, and Cr-white mica (fuchsite/mariposite) forms through potassium metasomatism of the country rocks (Uçurum, 2000). Listvenite is important since it is commonly associated with low-temperature Ag, Hg, As, Co and Ni mineralization worldwide (Buisson and Leblanc, 1986). Listvenite lode–gold associations are often located within or near major fault or shear zones, many of which are terrane boundaries (Halls and Zhao, 1995 and references therein).

In the central and southern parts of the Eastern Desert of Egypt, listvenite is commonly associated with highly tectonized, allochtho-nous ophiolitic serpentinites. Several studies reported significant gold concentrations in listvenite and listvenitized serpentinite (e.g., Botros, 1993; El-Dougdoug, 1990; El-Mezayen et al., 1995; Hassaan et al., 1996, 2009; Osman, 1995; Ramadan, 2002; Ramadan et al., 2005). The Barramiya district in the central Eastern Desert of Egypt hosts several gold occurrences with gold-bearing quartz veins mostly situated along the east–northeast-trending Barramiya–Um Salatit ophiolitic belt. The Barramiya deposit is a vein-type gold–arsenic mineraliza-tion, associated with listvenite, close to chromite, magnesite and antimony ores (Sabet and Bondonosov, 1984). In the Barramiya district, listvenite is closely associated with sheared serpentinite at fault intersections or along the basal décollement of the major thrusts, especially where granitoid massifs and stocks are common. Occasional high gold contents (up to 11 ppm) have been reported in some samples of the highly ferruginated/silicified listvenite in the mine area (Osman, 2001). Adjacent to the quartz veins, grab samples of talcous graphite-bearing slate, densely seamed with quartz veinlets and disseminated sulfides, gave anomalous high gold values of 2.7 g/t Au (Botros, 2004 and references therein). Mining activities were sporadic since Pharaonic times until the twentieth century, but the deposit has been completely abandoned in 1961 (Gabra, 1986; Kochine and

* Corresponding author. Tel.: +20 132711911; fax: +20 133222578.
E-mail address: basem.zoheir@gmail.com (B. Zoheir).

Basyuni, 1968 and references therein). The worked orebodies were mainly sulfide-bearing quartz and quartz–carbonate lodes associated with listvenite exposures, showing signs of structural control expressed in preferable orientation and consistent meso- and microfabrics.

In the present study, field work, mineralogical investigations, fluid inclusions and stable isotope studies are aimed at better understand of the genesis of the Barramiya gold deposit in relation to listvenite. We also focus on the structural control of the mineralization and conditions of gold deposition.

2. Geologic and structural settings

The basement complex of the Barramiya district comprises Neoproterozoic ophiolitic mélange of allochthonous blocks and clasts of serpentinite and carbonatized/silicified derivatives tectonically incorporated in variably deformed metasedimentary and volcani-sedimentary rocks (Fig. 1). These rocks are covered in the western part of the map area by the Cambrian–Upper Cretaceous Nubian Sandstone. Serpentinite, along with relict harzburgite, pyroxenite and subordinate metabasalt, form the hilly Barramiya–Um Salatit belt elongated in an ENE trend concordant with the main foliation of the ophiolitic mélange matrix. Along the thrust zones, talc, magnesite and chromite form veinlets, nodules or irregular pockets in the sheared ultramafic rocks. Listvenite is exposed as a several hundred meters long, ~100 m-wide elongate body at the mine area along an ~E–W-trending dextral fault and adjacent to a sheet-like granitoid body (Fig. 2). Listvenite is composed of Fe–Mg carbonate, quartz and Cr-bearing white mica, together with disseminated chromite and accessory pyrite. It is characterized by pale green to yellowish green color; the reddish brown surface appearance is ascribed to oxidation of Fe-bearing carbonate to iron oxides. Tectonized serpentinite is altered to listvenite through talc-actinolite schist and talc carbonate

rock as the intensity of carbonatization increases near steeply dipping transpressive faults (Fig. 3a).

Successions of finely banded quartz–sericite and graphite-bearing quartzo-feldspathic schists admixed with metagreywacke and -siltstone are locally intercalated with lenticular bodies of massive and tectonized serpentinite, tremolite-talc schist and listvenite (c.f. El-Shazly, 1977). These tectonically admixed sedimentary/volcani-sedimentary and ophiolitic rocks form the ophiolitic mélange matrix in the area. The island arc metavolcanic/volcaniclastic rocks of mainly andesitic and basaltic–andesitic composition cover a vast terrain in the southern part of the map area. Deformed gabbro-diorite rocks cut the ophiolitic mélange matrix and island arc metavolcaniclastics in the eastern part of the study area. On the other hand, several 10s km-across intrusions of heterogeneously foliated, syn-orogenic quartz–diorite/granodiorite cut through the ophiolitic rocks in the northern part of the study area. At the mine area, intensively weathered granite porphyry and elongate (E–W) granodiorite bodies cut the main foliation of the mélange matrix. Discrete elongate bodies of post-orogenic monzogranite and granite porphyry are bound to intersection zones of steeply dipping E–W and NW–SE trending faults (Fig. 3b). Post-granite dykes including quartz porphyry, rhyolite, dacite and less common basalt are oriented in different directions in the mine area.

Superimposed structural elements indicate a complex deformation history of the Barramiya region. An early folding phase (F_1) is best developed in the metasedimentary rocks in the central part of the study area. Penetrative foliation S_1 (ENE–WSW) axial planar to F_1 folds dips moderately (58–69°) to NW (Fig. 3c). Major, ENE-trending thrust structures border the large, elongate ophiolitic slabs and are commonly associated with F_1 folds. Tight to isoclinal or overturned folds (F_2), and related NW–SE ductile shear zones are developed in the ophiolitic rocks, where S_2 is defined by preferably oriented chlorite flakes and actinolite laths. Asymmetric crenulations and kink bands (F_3), and locally
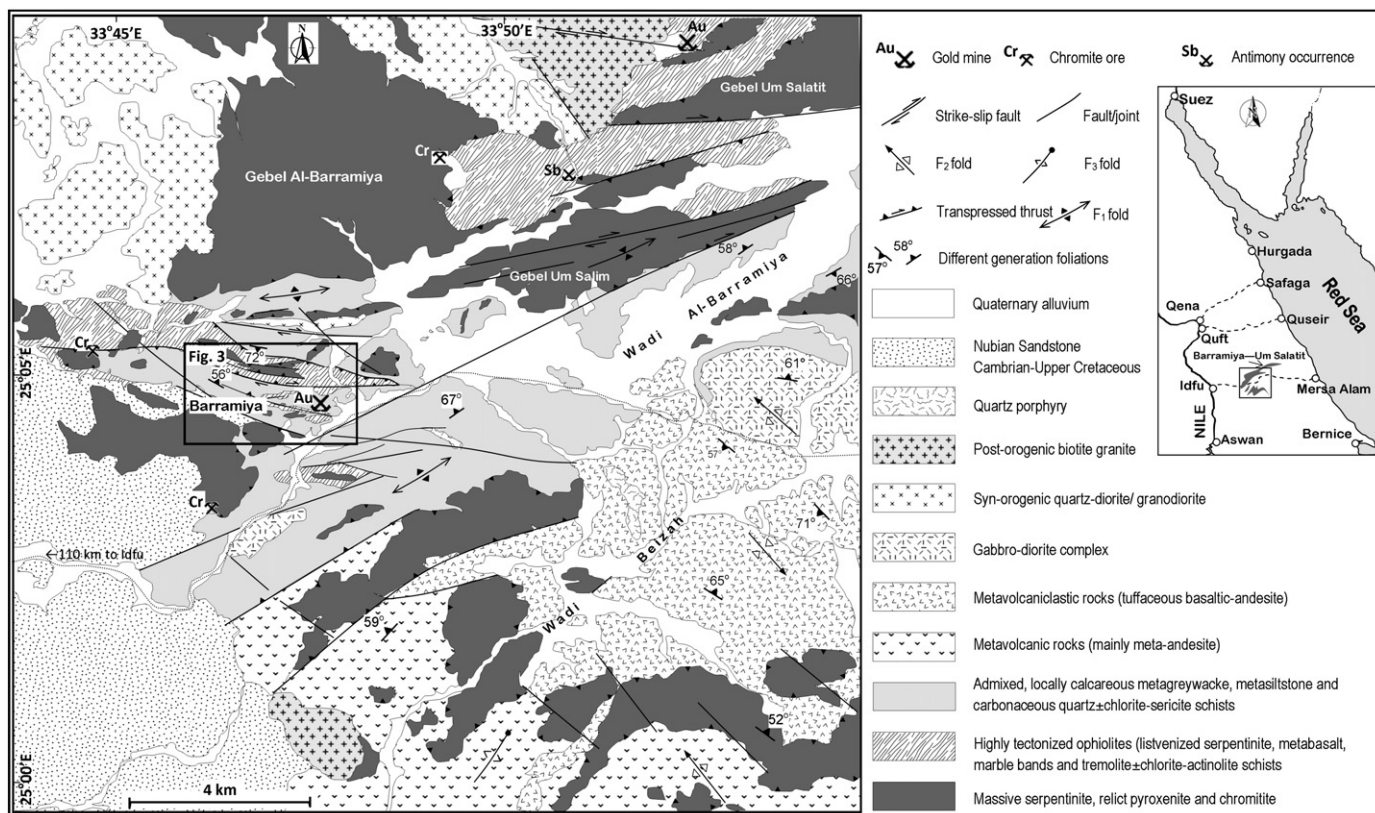

Fig. 1. Geological map of the Barramiya area (modified from Botros, 2004; EGSMA, 1992; El-Shazly, 1977; Gabra, 1986). Inset showing a location map.
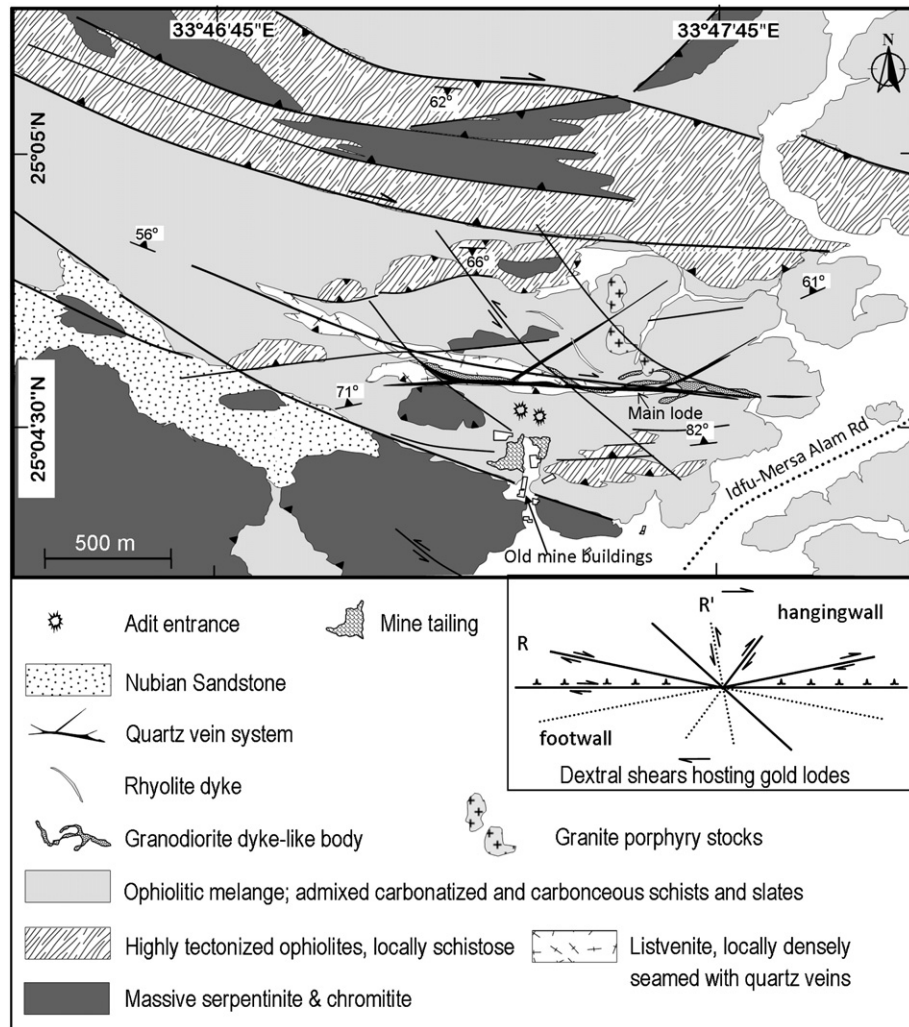
Fig. 2. Detailed geological map of the Barramiya gold deposit.

penetrative foliations (S₃) are attributed to a third stage in the ductile deformation history of the area. F₃ folds have NE–SW axial planes and dip gently or moderately to SE. Dextral transpression along the major thrust planes together with discrete, commonly km-scale shear zones took place subsequent to the development of F₂ folds and was likely coeval with F₃ folds. Consistent asymmetry of the locally developed shear cleavages demonstrates an east-side-up sense of shear along the NNW–SSE shear zones, and a right-lateral offset along the ESE–WNW and NE–SW shear zones. In the mine area, auriferous quartz and quartz–carbonate veins and altered wallrock gouge occur where these ESE–WNW and NE–SW shear zones cut through a listvenite block adjacent to an elongate granodiorite body (Fig. 3d).

3. Gold mineralization

The mineralized quartz and quartz–carbonate veins are associated with E–W shear zones and related splays and relays. This shear system cuts across the main foliation in the graphite-bearing schists and chlorite–actinolite schists (N74°E/67°NW). Most veins range in thickness from 10 cm to 1 m, and extend for lengths between a few meters and 1 km along strike and up to 400 m along dip (Gabra, 1986). The bulk oreshoots are central shear veins and Reidel shear fracture infillings controlled by a fault/fracture pattern that defines a right lateral shear system (see Fig. 2). The mineralized quartz lodes and associated sub-parallel veinlets form a vein system reaching

15–20 m in thickness. On the vein walls and along the fault planes, discrete vertical slickensides disrupt the horizontal slip striae, or are locally deformed by oblique striations, implying a subsequent dip-slip movement (see Fig. 3d). On the other hand, some barren milky quartz veins are accommodated in steeply dipping NW–SE extensional fractures.

The orebodies are made up of early bluish/grey quartz fractured and sealed with a late milky quartz phase (Fig. 4a), or mainly of milky quartz with appreciable amounts of Fe-carbonate and wallrock materials (Fig. 4b). The gold content in quartz vein varies from traces up to 18 ppm (Kucha et al., 1998). Most veins exhibit boudinage structures along the strike and dip, and taper off at ends. Stylolitic and sheeted structures are common where slivers of carbonaceous wallrocks are associated with elongate quartz ribbons (Fig. 4c). Vugs and open-space filling textures have not been observed, however, dilational bends are abundant in the carbonaceous schists, in which kinks are common. Occasionally, the E–W quartz veins are affected by open F₃ folds (Fig. 4d).

The chief constituents of the ore bodies are quartz, carbonate minerals, and altered wallrock gouge. At least two generations of quartz comprise the veins, commonly attested by (a) ribbon and brecciated milky or bluish-grey quartz sealed with (b) massive milky quartz ± carbonate (see Fig. 4a). Carbonate minerals are widespread throughout the veins and display a wide range of compositions. Ankerite is the dominant carbonate phase throughout the quartz
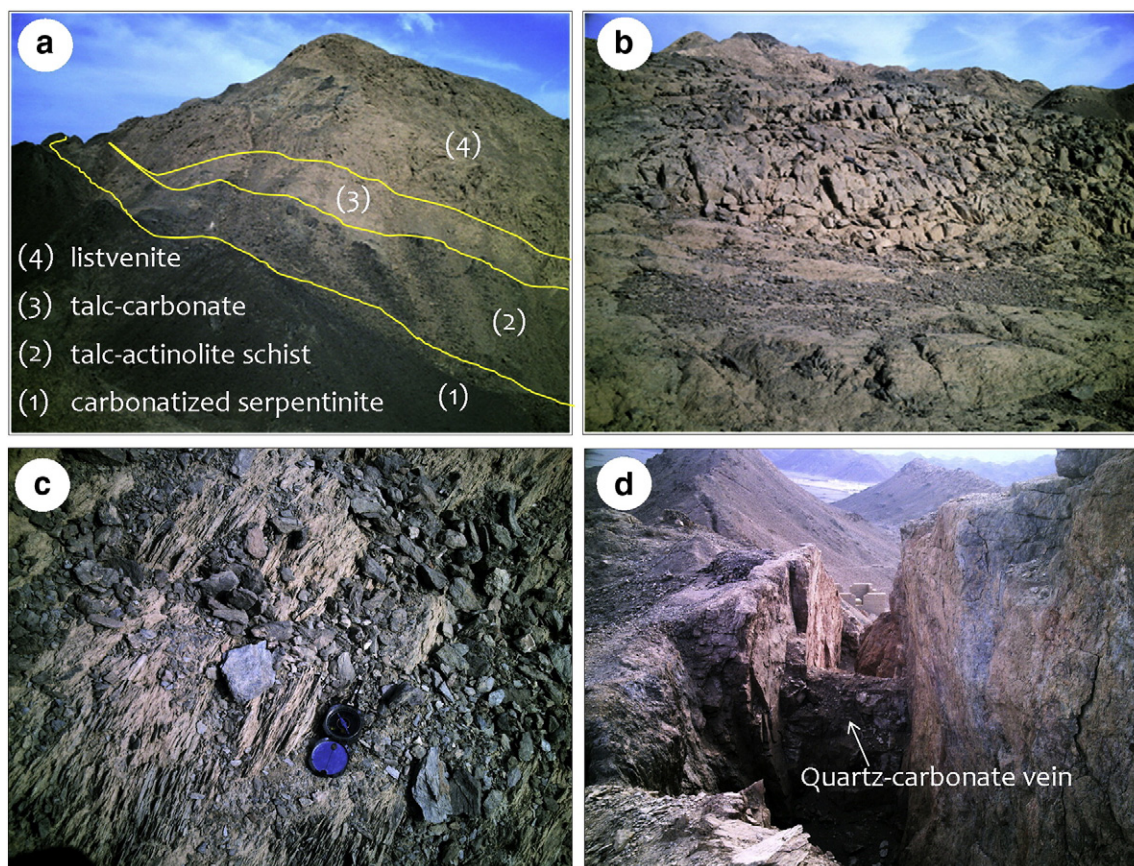
Fig. 3. Field relationships at the Barramiya mine area. (a) — Variably deformed, carbonatized ultramafic rocks progressed into listvenite (View looking W), (b) — Highly altered granite porphyry north of the vein system (View looking N), (c) — S₁ foliation (N52°E/78°NW) best preserved in the actinolite–tremiloite schist adjacent to the tectonized serpentinites, (d) — ENE–WSW oriented mineralized quartz–carbonate vein of considerable width. Notice the oblique slickensides on the northern vein wall (view looking E).

veins, commonly rimming selvages of the wallrocks (Fig. 5a). Less commonly, aggregates and fibers of magnesite–siderite ± calcite occur as replacement phases filling the open vugs in some veins, and are associated with comb quartz. Other gangue minerals include sericite/mariposite, goethite, rutile and limonite. The wallrock selvages comprise carbonatized actinolite schist and listvenite, with or without carbonaceous material (Fig. 5b). These selvages are rich in disseminated pyrite–arsenopyrite–chalcopyrite and are characterized by microbrecciation, slip, and annealing textures. An assemblage of chlorite ± graphite–carbonate minerals occupies the serrate planes between deformed quartz crystals, outlining a distinct stylolitic texture (Fig. 5c, d).

Vein quartz displays variable degrees of shearing, manifested by strong to moderate undulatory extinction, stretched quartz ribbons, and recrystallized bulges along larger quartz crystal boundaries (Fig. 6a, b). In the laminated quartz veins, quartz crystals show mixed plastic and brittle deformation. Cores of the large quartz grains are sutured and exhibit smooth undulose extinction instead of sharp deformation bands. Most gold-sulfide mineralization is confined to the stylolitic planes in recrystallized quartz veins, where disseminated sulfides are associated with a carbonaceous material (Fig. 6c). Where granulated and brecciated, quartz is sealed with a network of calcite (Fig. 6d).

4. Methods

Mapping of the Barramiya district was based on field work, geometrically corrected and balanced satellite (ETM+) images and compilation of the available previous work including regional maps. The detailed map of the mine area aims at illustrating the relationship

between the auriferous shear zones and the regional structural elements. Principal component analysis and band ratio techniques were applied for the geological mapping and accurate discrimination of the alteration zones. For mineralogical and fluid inclusion studies, a representative set of samples (~130 lodes and host rock samples) has been collected from the surface and underground work in the mine area and surroundings. Petrographic examination and preliminary mineral identification were done on polished and thin sections using a Zeiss Axion microscope and by SEM back-scattered electron imaging. Quantitative electron microprobe analyses of major and minor elements were obtained with a Cameca SX100 four spectrometer, fully automated electron microprobe using wavelength-dispersive X-ray spectrometry. Analyses of sulfide minerals were made at 30 keV accelerating voltage and 40 nA (and 300 nA for Au, Sb, Ag, Ni, and Co) beam current, and counting times of 10 to 300 s, using a 2 μm diameter probe spot. Natural and synthetic sulfides were used as reference materials. Relative accuracy of the analyses, based upon comparison between measured and published compositions of standard reference materials, is ~1–2% for concentrations >1 wt.% and ~5–10% for concentrations <1 wt.%. Element detection limits (wt.%) at the three sigma level were As (0.02), Cd (0.03), Co (0.01), Cu (0.02), Fe (0.01), Mn (0.01), Pb (0.15), S (0.02), Ni (0.01), Sb (0.02), V (0.01), Au (0.006), Ag (0.01) and Zn (0.03). Carbonate minerals, sericite and chlorite were analyzed in samples of wallrock and quartz veins. Operating conditions were typically 15 kV, 20 nA beam current and a 2 μm beam diameter.

Fluid inclusion microthermometric measurements were carried out on a Linkam THMSG 600 heating–cooling stage at the Institute of Mineralogy and Mineral Resources, Technical University of Clausthal
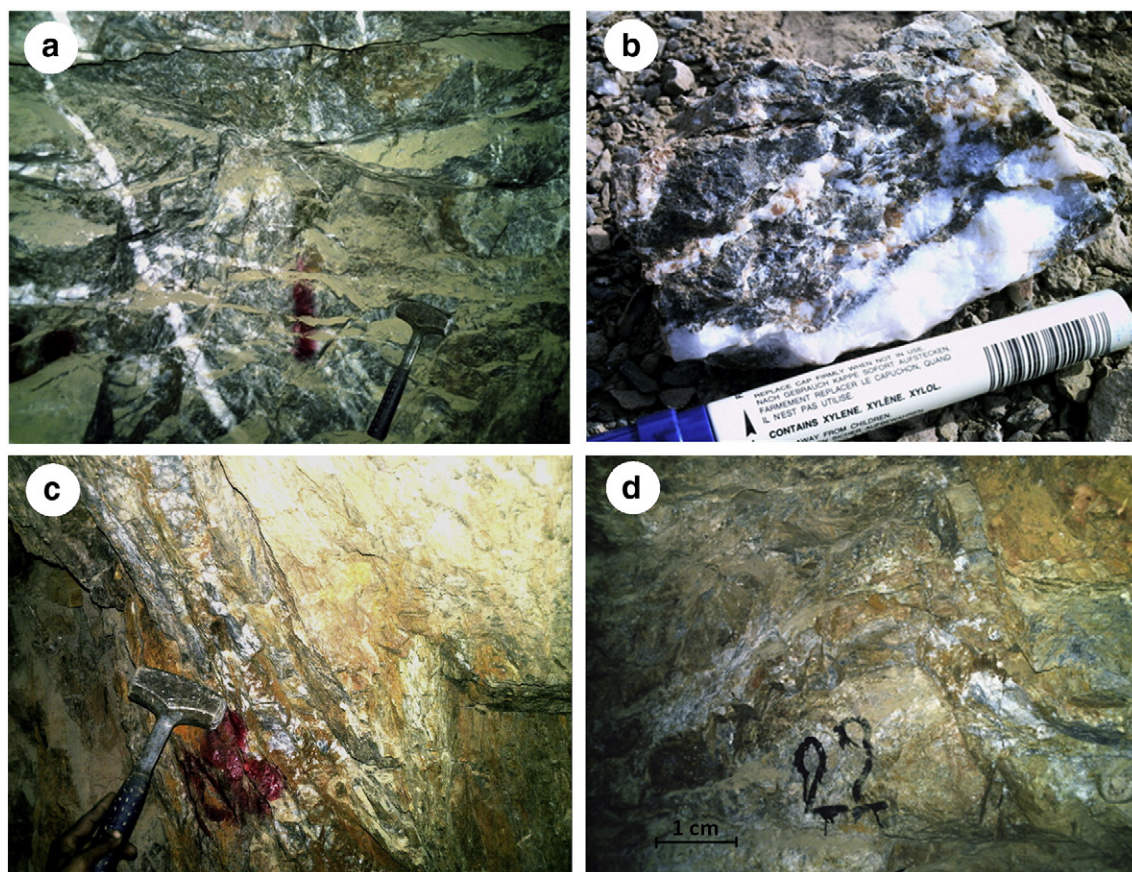
Fig. 4. Features of the mineralized quartz veins at the Barramiya mine, (a) — Main Lode made up mainly of a voluminous early bluish quartz phase and a late fissure-filling milky quartz phase, (b) — Hand specimen of the NE–SW trending lodes with abundant Fe-carbonate and wallrock selvages, (c) — Sheeted quartz lode with abundant wallrock materials (view looking W), (d) — Markedly deformed, folded quartz–carbonate vein.

(Germany). Additional information on fluid inclusions was obtained by Laser Raman Spectrometry (LRS) at the Section of Mineralogy and Mineral Resources, University of Geneva (Switzerland). A full suite of the electron probe microanalysis (EPMA) and fluid inclusions data is available on request from the corresponding author.

Several sulfide grains have been analyzed for their major and some trace elements by a laser ablation inductively coupled plasma mass spectrometry (LA-ICP-MS) at The University of Erlangen (Germany). High precision spatially resolved analysis of δ^{34}S in sulfides has been accomplished using a laser ablation system linked with a multi-collector (MC)-ICP-MS at the Scottish Universities Environmental Research Centre (SUERC), UK.

5. Ore mineralogy, paragenesis and arsenopyrite geothermometry

5.1. Ore minerals

Ore minerals disseminated in the quartz veins and adjacent wallrocks are mainly arsenopyrite, pyrite and trace amounts of chalcopyrite, sphalerite, tetrahedrite, galena, pyrrhotite, gersdorffite and gold. Partial to complete replacement of pyrite by marcasite is common. Other secondary phases include covellite and goethite. Sulfides generally make up less than 2% of the vein volume, but vary in abundance across the width of the vein. Arsenopyrite and pyrite occur as medium to fine-grained disseminated grains (tens of μms to 0.5 cm wide) throughout the veins, but also as clusters intergrown with chalcopyrite. Generally, these ore minerals are most abundant along the carbonaceous shear planes in the wallrocks or in domains rich in Cr-sericite (mariposite) and Mg–Fe-carbonate in the quartz veins.

Arsenopyrite is ubiquitous in quartz lodes and mineralized wallrock (Fig. 7a). It is generally optically homogeneous, but many of the large crystals (≥150 μm) display porous or inclusion-rich (sphalerite, chalcopyrite, gersdorffite and gold) cores and homogenous rims. Electron microprobe analysis of arsenopyrite revealed As-contents ranging from 40.1 to 43.6 wt.%, and occasionally elevated Ni, Ag, Sb, and Au contents (Table 1). Refractory gold in arsenopyrite, commonly at 100s ppm range and less frequently >1000 ppm Au, is evident by the electron microprobe and LA-ICP-MS analyses (n = 102, range 2193–116 ppm, average 667 ppm Au). Pyrite occurs as dispersed coarse hypidiomorphic or xenomorphic crystals and aggregates intergrown with arsenopyrite. Most of the large pyrite grains reveal local cracking and cataclasis or are pseudomorphed by marcasite, commonly where chalcopyrite and digenite are abundant (Fig. 7b). Traces of Ni (up to 0.69 wt.%), As (up to 0.67 wt.%), Cu (up to 0.61 wt.%) and occasional hundreds of ppm Au are indicated by electron microprobe analysis of As-bearing pyrite (Table 1). Pyrrhotite occurs mainly as inclusion phases in pyrite and arsenopyrite, whereas free grains are relatively rare.

Chalcopyrite occurs as anhedral crystals replacing pyrite and arsenopyrite and is intergrown with sphalerite and less common galena (Fig. 7c). Tetrahedrite occurs as subhedral crystals intergrown with chalcopyrite, and as minute inclusions in large chalcopyrite grains. Chemical data of tetrahedrite from the Barramiya deposit (Table 1) indicate a generally silver-rich, iron-poor composition (freibergite). Silver content in the analyzed grains varies from 29.45 to 36.89 wt.%, and Sb content varies from 21.1 to 27 wt.%. Au content in tetrahedrite varies from traces up to >1000 ppm. Sphalerite and galena are commonly intergrown with chalcopyrite in comb quartz domains (Fig. 7d). Electron microprobe results on chalcopyrite and galena show that they are close to stoichiometric composition.
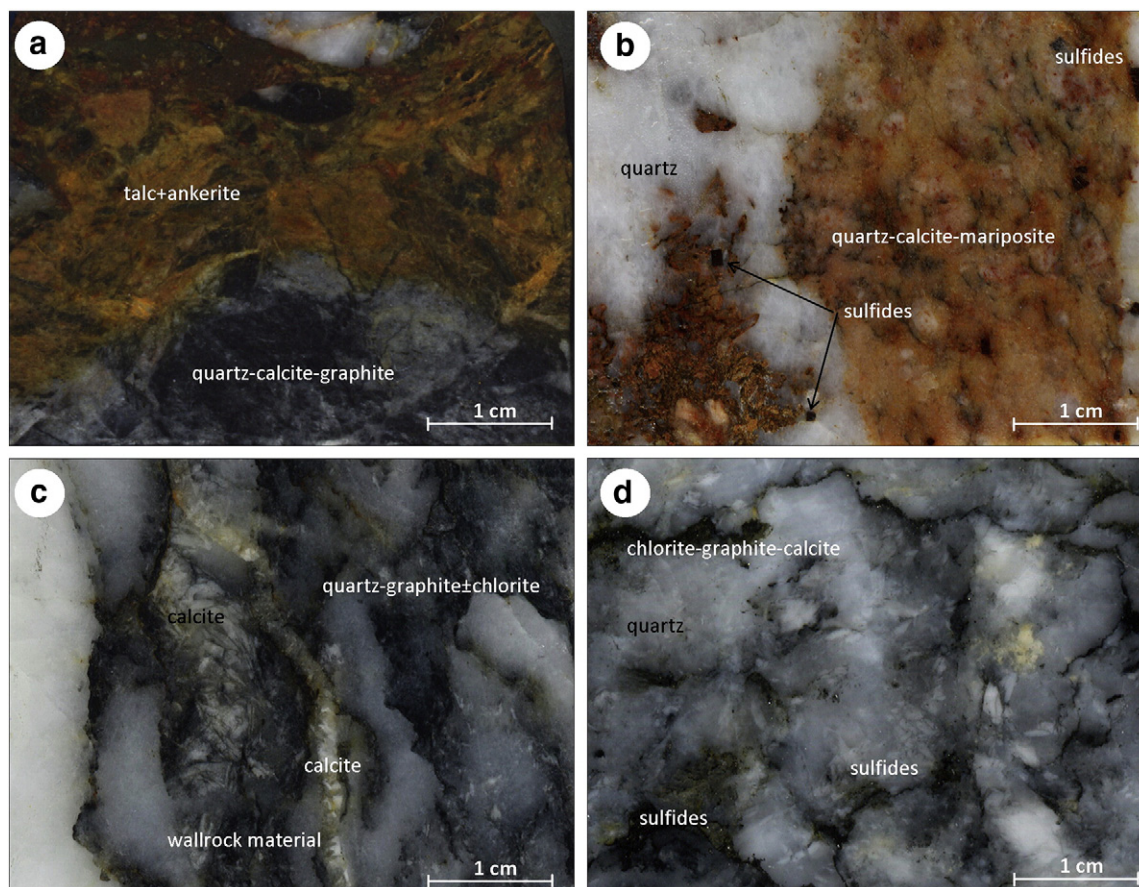
Fig. 5. Features of the mineralized quartz veins from the Barramiya deposit. (a) quartz vein composed essentially of quartz and selvages of talc-carbonate rocks, (b) mineralized lode made up of quartz–listvenite and disseminated sulfide mixture, (c) laminated quartz vein with alternated quartz and carbonaceous material-rich lamina, notice the late calcite vein sealing fractures parallel to the lamina, (d) stylolites coated with chlorite–carbonate and carbonaceous material in grey quartz vein with abundant disseminated sulfides.

Sphalerite composition is very uniform with Fe varying from 2.5 to 3.6 wt.%, and 4 to 6 mol% FeS. Cu varies from 0.98 to 1.96 wt.%; Cd, Ni and As are below or around the detection limit. Neither stibnite nor antimony sulfosalts have been observed.

Although visible gold is rare, microscopic and submicroscopic free-milling gold grains occur as dispersed blebs and specks along fine ribbons of wallrock in quartz veins, and in the graphitic shear planes. These wallrock selvages are the locus of abundant fine-grained arsenopyrite that is frequently intimately associated with gold. Inclusions of gold (~10 μm-across) have been observed in the As-bearing pyrite grains intergrown with arsenopyrite (Fig. 7e), or occur as free grains embedded in the quartz–sericite–ankerite selvage. Typical free gold grains contain considerable to little silver (74–93 wt.% Au).

Deformation of the early sulfide assemblage, especially arsenopyrite and pyrite is variable but distinct in kinked wallrocks, where contorted and pseudomorphosed grains are observed (Fig. 7f). Based on the ore textures including intergrowth and replacement, a two stage-mineralization paragenesis is suggested for the Barramiya deposit (Fig. 8). During the early mineralization stage, arsenopyrite, gersdorffite, pyrrhotite and pyrite have been formed, followed by chalcopyrite, tetrahedrite, sphalerite and galena in the late mineralization stage. The bulk sulfide mineralization was overprinted by a late, variably pervasive secondary alteration.

5.2. Arsenopyrite geothermometry

The internal chemical homogeneity of arsenopyrite in the Barramiya deposit allow the application of the arsenopyrite geothermometer

(Kretschmar and Scott, 1976; Sharp et al., 1985) on arsenopyrite crystals intimately associated with gold and/or containing up to several hundreds of ppm Au. The compositional data on the Barramiya auriferous arsenopyrite (29.4–31.2 at.% As) indicate a temperature range of 317–376 °C based on the phase diagram given by Kretschmar and Scott (1976). Strongly auriferous arsenopyrites (arsenopyrite with hundreds of ppm Au) has 30.4–31.1 at.% As, implying a temperature range of 325–370 °C. The composition of disseminated gersdorffite (67–79 mol% NiAsS, 20–33 mol% FeAsS, and traces of CoAsS) intimately associated with gold corresponds to sulfarsenide and must have crystallized or re-equilibrated at 320–460 °C (Klemm, 1965).

6. Gangue hydrothermal phases in lodes and wallrock selvages

Detailed examination of the gangue minerals associated with ore minerals is provided to add to the mineralogical context of the investigated gold mineralization. Gangue phases in the Barramiya deposits include quartz, sericite, carbonate and subordinate chlorite and rutile. Rutile occurs as specks, laths and patches disseminated in the pervasively altered wallrock, and within the carbonaceous stylolites in the sulfide-bearing laminated quartz veins.

6.1. Sericite

In the Barramiya deposit, sericite is generally silica-rich, and frequently Cr-bearing (mariposite–fuchsite). The term fuchsite has been used for the distinctive bright green, chrome-rich, phyllosilicate phase. The nomenclature of chrome micas is not entirely clear (Bailey,
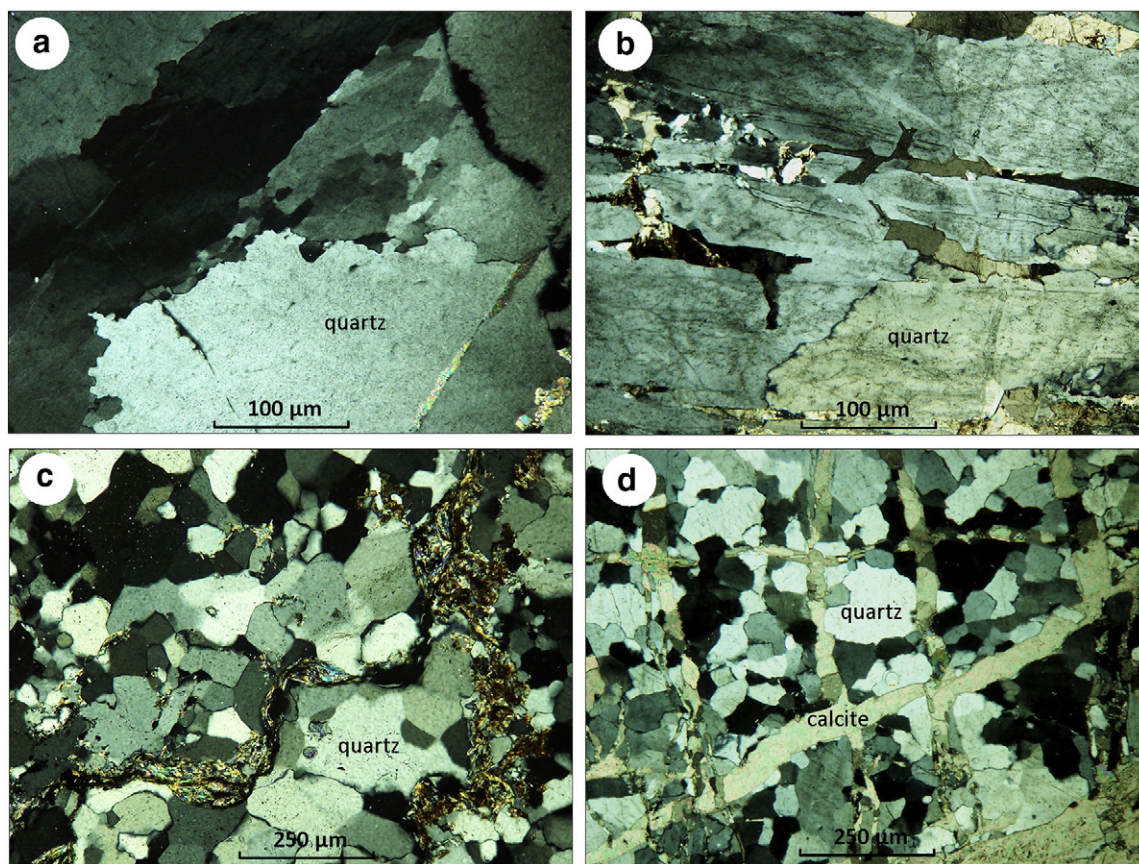
Fig. 6. Quartz textures of the mineralized quartz veins from the Barramiya deposit. (a) Moderate undulose extinction in stretched quartz ribbons, with sutured boundaries, (b) Sheared, recrystallized quartz ribbons with small bulges at boundaries, (c) Recrystallized quartz and stylolites filled with sericite–chlorite–carbonate ± graphite and sulfide minerals, (d) Calcite occupies healing fractures in recrystallized quartz veins.

1984), with fuchsite used for sericite containing more than 1 wt.% Cr_2O_3 (Deer et al., 1962) but mariposite used for both low-Cr sericites and Cr-rich phengites (Heinrich, 1965). In the Barramiya listvenite, Cr_2O_3 contents of sericite vary from traces to 1.16 wt.% (Table 2), but more frequently between 0.5 and 0.8 wt.%, and therefore could be classified as mariposite. The source of chromium is most likely the alteration of Cr-rich clinopyroxenes or hydrolysis of chromite (cf. Savage et al., 2000) from an ultramafic protolith. The structural formulae of sericites show tetrahedral Si varying from 6.41 to 6.96 apfu. $Al^{(IV)}$ varies from 1.04 to 1.59, $Al^{(VI)}$ from 3.28 to 3.83, K from 0.61 to 1.25, Mg from 0.22 to 0.74, Fe from traces to 0.17, Na from 0.02 to 0.06, and Cr from 0.01 to 0.12 apfu. All other elements occur in small quantities (Table 2).

6.2. Carbonate minerals

Carbonate minerals are present in the wallrocks as patches in the matrix and as replacements of chlorite, actinolite and/or serpentine. They also occur as veinlets in quartz veins and in the matrix of the adjacent wallrocks. Most of the carbonate minerals analyzed by EPMA are restricted to either dolomite–ankerite or ferroan magnesite (breunner-ite) compositions (Table 3). However, an early complete magnesite–siderite series is observed in a few samples, likely as solid solution (Table 3). Following Buckley and Woolley (1990), the boundary between dolomite and ankerite is taken at Fe/Mg = 0.25, and the magnesite–siderite series is subdivided at Mg:Fe ratios of 0.75, 0.5 and 0.25 into magnesite, ferroan magnesite (breunnerite), magnesian siderite (side-roplesite) and siderite. This early genetic assemblage is partly replaced later by calcite in lodes and adjacent wallrocks. Ferroan dolomite occurs as coarse patches in quartz lodes, as veinlets, and as fine-grained replacement phase disseminated within the mineralized wallrocks

which form a broad selvage to the sulfide-bearing veins. Manganese contents are generally low (<2 wt.% MnO). EPMA data indicate that contents of FeO and MnO in ferroan dolomite are generally higher in veinlets than in disseminated ferroan dolomite grains. Breunnerite [(Mg, Fe)CO_3] is closely associated with disseminated sericite and sulfides in wallrocks and quartz veins. Variation in composition from dolomite/ ankerite to ferroan magnesite within individual samples is distinct.

6.3. Chlorite

Chlorite forms aggregated flakes associated with sericite and talc in the carbonatized serpentinite, or fills microfractures in vein quartz. Chlorite is also common along the stylolitic planes in quartz veins. The microprobe data show that the analyzed chlorites have generally homogenous Mg-rich compositions (Table 4). Chlorite is notably much abundant in selvages of the host rocks enclosed in quartz veins than in wallrocks bordering the quartz veins. This observation may support a hydrothermal origin of this chlorite.

7. Fluid inclusions and sulfur isotope studies

No unequivocally primary isolated or clustered fluid inclusions were identified, consistent with the reactivation and multistage development of veins in the shear zone. Fluid inclusion studies were performed on the larger and better preserved quartz grains of quartz and quartz–carbonate veins. Recrystallized grains or grains suspected of having been modified were avoided in the microthermometric work. Inclusions occurring along intragranular trails along crystallographic planes in the vein quartz are chosen for measurements. These inclusions show commonly aqueous ± carbonic compositions with two or three phases
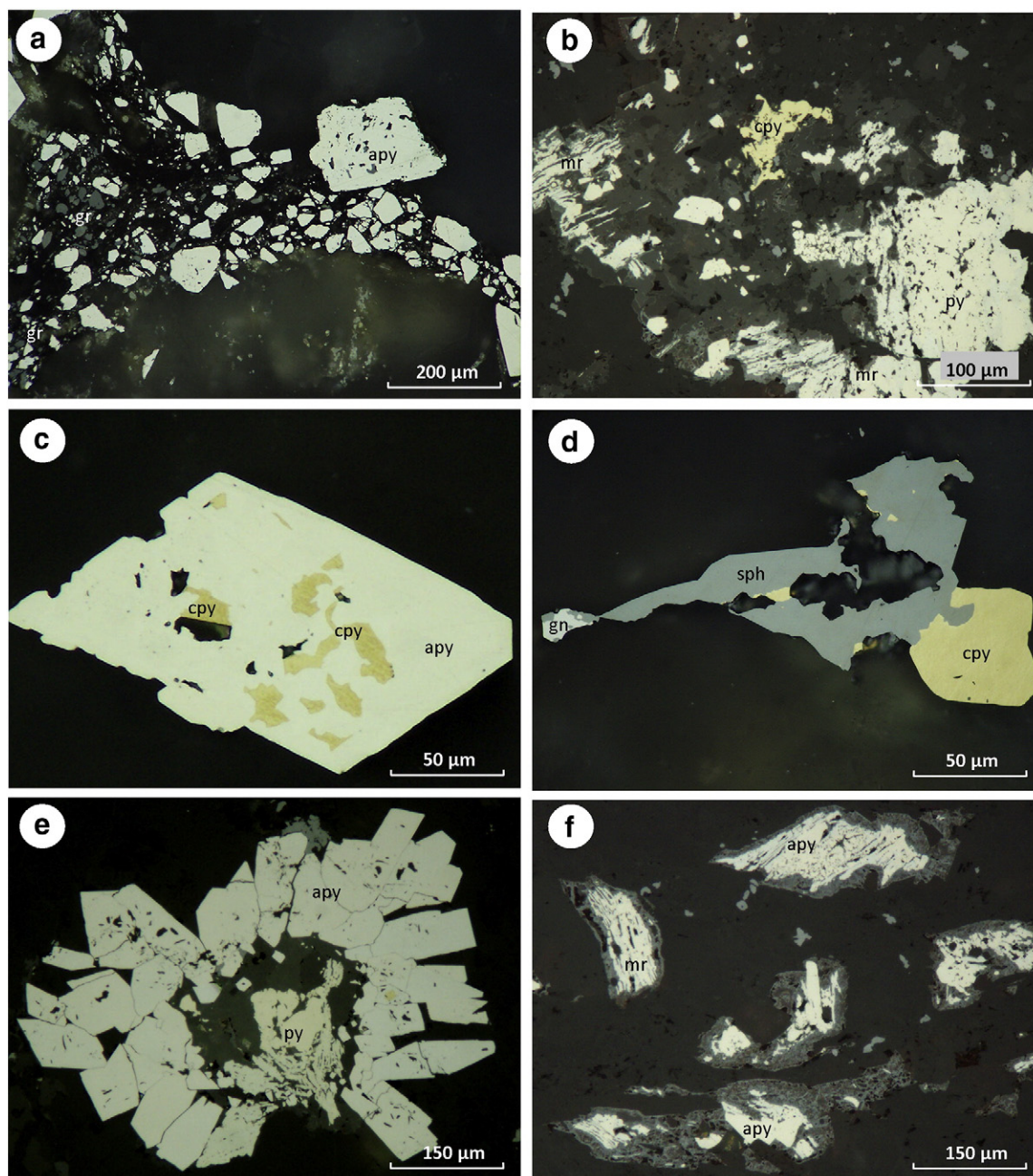
Fig. 7. Photomicrographs of selected polished sections from the Barramiya lodes (reflected polarized light, oil immersion) showing: (a) Disseminated arsenopyrite (apy) associated with carbonaceous material (c) along stylolitic planes in quartz vein, (b) Chalcopyrite (cpy) and pyrite (py) pseudomorphosed into marcasite (mr), (c) Arsenopyrite replaced by chalcopyrite, (d) Sphalerite (sph) intergrown with chalcopyrite and galena (gn), (e) Clustered arsenopyrite and As-bearing pyrite in a radial form, (f) Deformed arsenopyrite grains along foliation of the host carbonaceous schist.

at room temperature, and generally constant aqueous/vapor volume ratios in a single inclusion trail (0.3 to 0.4). Some inclusions contain minute solid phases, i.e. accidentally captured carbonaceous material. Less abundant, dark monophase, $CO_2 \pm CH_4$ inclusions (~2 µm) are associated with the aqueous-carbonic inclusions. Their small size did not allow for a microthermometric study. The aqueous-carbonic inclusions show polyhedral outlines or irregular shapes, with their longest dimensions ranging from 4 to 15 µm.

7.1. Microthermometry and Laser Raman data

The microthermometric behavior of both carbonic and aqueous-carbonic fluid inclusions upon cooling–heating runs includes: (a)

nucleation of a CH_4 gas phase within the bubble at temperatures <−118 °C and its subsequent homogenization to the liquid at ~−82 °C, (b) melting of solid CO_2 varying from −61.8 to −57.2 °C, followed by homogenization of CO_2 to liquid, between 7.3 and 19.2 °C (Fig. 9). A Few carbonic inclusions, with sufficient size for measurement, yield similar T_{mCO2} and T_{hCO2} values. The final dissolution of clathrate occurred mostly before the partial homogenization of the carbonic phase. Most inclusions have $T_{m\ clath}$ between 5.6 and 9.3 °C with >80% of the values clustering at 7 to 8 °C (Fig. 9a). This defines a salinity of 4.5 wt.% NaCl equiv. Few inclusions showed the dissolution of clathrate at temperatures higher than 10 °C, which can be attributed to the presence of CH_4 (Collins, 1979). The final homogenization of inclusions in each individual trail occurred in a relatively limited

Table 1
Representative EPMA data of sulfide minerals disseminated in the Barramiya quartz lodes and adjacent wallrocks.

Arsenopyrite

Fe	35.07	34.46	34.55	34.47	34.45	35.17	34.32	34.75	34.33	35.33	35.26	35.62	35.49	35.48	35.07
S	22.72	21.88	21.05	22.19	21.27	23.03	21.61	22.03	22.13	22.03	23.15	23.01	21.46	23.02	22.93
As	42.21	42.08	43.30	42.09	43.24	40.92	42.07	41.90	41.96	42.54	41.67	41.77	42.35	41.68	41.40
Ni	–	0.23	0.20	0.24	0.41	0.13	0.27	0.38	0.13	–	–	–	–	–	0.10
Cu	–	–	–	0.04	0.05	–	–	–	0.02	–	–	–	–	–	–
Ag	–	–	0.03	–	0.22	0.21	–	0.21	–	–	–	–	–	–	0.19
Te	–	–	–	–	–	0.04	–	–	–	–	–	–	–	–	–
Au	0.21	0.13	0.17	0.16	0.02	0.05	0.08	0.16	0.12	–	–	–	–	–	–
Sb	–	0.07	0.02	–	0.06	0.19	–	0.07	–	–	–	–	–	–	0.09
Sum	100.01	98.78	99.32	99.25	99.73	99.71	98.37	99.41	98.73	99.91	100.1	100.4	99.30	100.2	99.80

Pyrite

Fe	46.04	46.13	46.04	46.47	46.44	46.60	47.80	46.50	46.65	47.49	46.87	46.00	46.04	46.44	46.91
S	52.26	53.86	53.89	53.93	53.82	52.43	52.81	52.04	52.28	51.33	52.24	51.29	51.27	52.77	52.26
As	1.57	0.22	–	–	–	0.37	0.05	0.22	0.05	0.22	0.22	0.18	0.22	0.67	–
Co	–	–	–	–	–	–	–	–	–	–	–	–	–	–	–
Ni	–	0.69	0.14	0.04	0.09	0.05	0.11	–	–	0.06	0.23	–	0.20	0.33	0.14
Cu	–	–	–	–	–	–	–	–	–	–	0.61	–	–	–	–
Ag	0.04	0.04	0.05	0.04	0.04	–	0.04	–	–	–	–	–	–	–	0.03
Te	–	–	0.02	–	–	–	–	–	–	0.03	–	–	–	–	–
Au	0.09	0.02	–	–	–	0.03	0.06	–	0.02	–	–	–	–	–	–
Sum	99.95	100.3	100.0	100.5	100.4	99.51	100.8	98.79	99.04	99.15	99.40	97.48	97.58	99.95	99.25

Chalcopyrite / **Sphalerite**

	Chalcopyrite								Sphalerite						
Fe	29.97	30.39	30.68	29.85	30.80	30.60	30.77	29.93	3.56	3.23	3.36	2.51	3.18	3.08	3.04
S	34.73	34.88	34.30	34.42	34.61	34.25	34.79	35.27	32.31	32.71	32.44	32.67	32.53	32.59	32.56
As	–	0.10	0.48	0.33	0.40	0.45	0.34	–	–	–	–	–	–	–	–
Ni	–	–	0.08	–	0.32	0.30	0.29	0.02	–	–	–	–	–	–	–
Cu	33.85	33.21	33.39	33.75	33.06	33.90	33.07	33.81	1.04	1.96	0.98	1.04	1.29	1.35	1.20
Zn	0.05	0.03	0.04	0.06	0.03	0.05	0.03	0.03	62.43	60.74	62.51	62.48	62.04	61.94	62.24
Ag	0.04	0.04	0.02	0.04	0.04	0.04	0.03	0.05	–	0.02	–	–	–	–	–
Te	–	–	–	0.02	–	–	–	0.02	–	–	–	–	–	–	–
Au	0.09	0.12	–	–	–	–	–	–	–	–	–	–	–	–	–
Sum	98.65	98.66	98.99	98.47	99.27	99.59	99.39	99.12	99.36	98.65	99.44	98.76	99.05	98.98	99.06

Sb-bearing Fe-gersdorffite (Ni,Fe)AsS / **Tetrahedrite–freibergite** / **Gold**

	Sb-bearing Fe-gersdorffite (Ni,Fe)AsS						Tetrahedrite–freibergite					Gold			
Fe	9.26	6.61	8.71	7.87	9.69	10.70	3.78	3.29	3.59	3.80	4.12				
S	19.96	19.55	19.80	19.74	19.95	19.88	17.39	17.27	17.21	16.98	16.17				
As	46.14	45.96	45.86	45.76	46.82	46.17	0.54	0.57	0.56	0.26	0.58				
Co	0.69	0.50	0.62	0.60	0.66	0.64	–	–	–	–	–				
Ni	22.37	26.68	24.48	25.52	21.30	22.32	–	–	–	–	–				
Cu	–	–	–	–	–	–	21.97	21.39	21.72	21.36	21.90				
Zn	–	–	–	–	–	–	>1.32	>2.16	1.62	1.10	0.96				
Ag	–	–	–	–	–	–	31.45	30.59	30.91	31.54	29.45	12.60	12.47	11.69	7.27
Te	–	–	–	–	–	–	–	–	–	–	–	–	–	–	–
Au	–	–	–	–	–	–	0.23	0.11	–	–	–	86.72	87.51	87.89	92.31
Sb	0.16	0.24	0.19	0.20	0.15	0.17	24.96	24.73	24.77	25.44	25.33	–	–	–	–
Sum	98.60	99.56	99.68	99.71	98.60	99.89	101.4	100.0	100.4	100.5	98.51	99.32	99.98	99.58	99.58

– below detection limit.

range of temperatures, commonly between 337 and 362 °C with a pronounced cluster around 350 °C. Bulk compositions, density, and isochores were calculated from microthermometric and Raman data using the Flincor program (Brown, 1989) and the equation of Bowers and Helgeson (1983) for the aqueous-carbonic inclusions. The carbonic phase is composed of a mixture of variable proportions of CH_4 and CO_2, an interpretation confirmed by micro-Raman spectroscopy (Fig. 9b, c). The bulk composition of the aqueous-carbonic inclusions based on the microthermometric measurements and Raman data is X_{CO2}: 4–43 mol% (typically 25–40 mol%); X_{H2O}: 55–96 mol% (typically 65–80 mol%); X_{CH4}: <15 mol%; X_{N2}: <4 mol%; and X_{NaCl}: 1–2 mol%. CO_2 densities vary from 0.78 to 0.88 g/cm^3; bulk densities are mainly in the range of 0.86–0.99 g/cm^3; and salinity varies from 1.5 to 8.2 wt.% NaCl equiv.

7.2. P–T conditions

The presence of CH_4 and/or N_2 in the CO_2–H_2O–salt system may affect some microthermometric properties and can cause misestimate of fluid salinity, density, and trapping pressures (Van den Kerkhof and Thiéry, 2001). However, the consistency of the salinity data precludes significant influence of the CH_4 and N_2 contents, except for a few T_{mclath} values >10 °C that are likely related to the presence of appreciable amounts of CH_4. As such, the salinities determined from the largely predominant group of inclusions are considered as good estimate of the composition of the ore fluid. Using the isochores for the aqueous-carbonic inclusions, the formation temperatures of the auriferous quartz lodes range from 325 to 370 °C under pressures of 1.3–2.4 kbar (Fig. 9d).

7.3. Entrapment mechanism

Criteria including comparable T_{hCO2} and T_{mCO2} ranges of the aqueous-carbonic and carbonic inclusions, presence of similar amounts of $CH_4 \pm N_2$ in both types, and their identical Raman data suggest that these inclusions trapped the same fluid as synchronous inclusions (sensu Fonarev et al., 1998). Variations in phase ratios, temperature of homogenization of the carbonic phase and in total
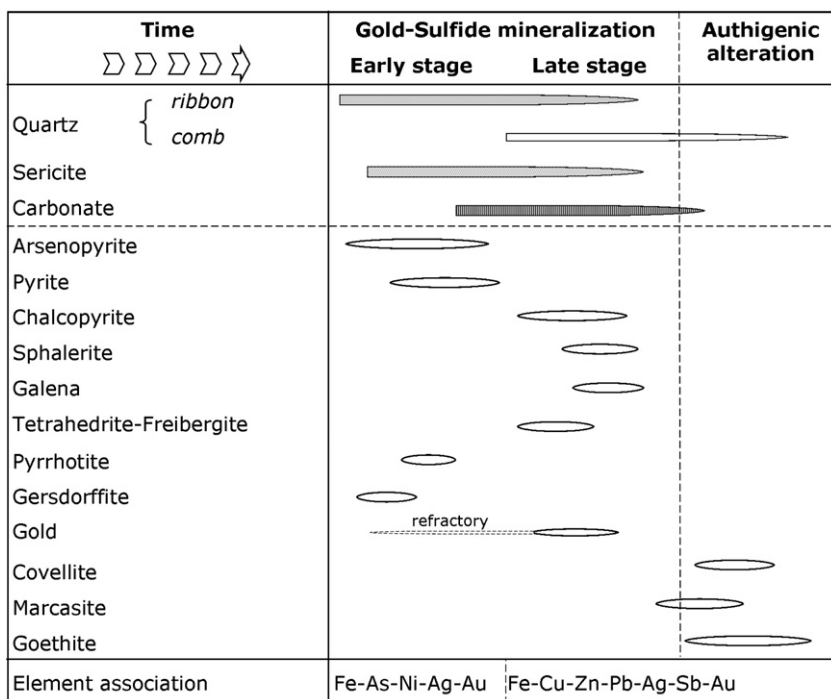
Fig. 8. Paragenetic sequence of the Barramiya gold deposit based on petrographic examination and SEM analysis. Large ovals represent major phases and small ovals represent minor phases.

homogenization temperatures of coexisting inclusions are typical of heterogeneous entrapment. This may be produced either by entrapment of immiscible fluids (mechanical mixture of two end members; Anderson et al., 1992) or when an initially homogeneous fluid undergoes effervescence (e.g., Diamond, 2001). The absence of coeval

and spatially related aqueous inclusions and the correlation between final homogenization temperatures and salinity (Dugdale and Hagemann, 2001) preclude mixing. In addition, homogenization of the aqueous-carbonic inclusions consistently into the liquid state, and the asymmetric frequency distribution of the partial and total

Table 2
Representative EPMA data of sericite disseminated in quartz lodes and listvenite selvages.

Point	1/1	2/1	3/1	11/1	12/1	13/1	14/1	15/1	16/1	18/1	21/1	37/1	38/1	39/1	40/1	41/1
SiO_2	53.11	52.45	53.22	53.13	52.24	54.61	53.60	53.03	49.61	51.30	51.53	51.96	51.91	51.75	51.66	52.53
TiO_2	–	–	–	–	–	0.07	–	–	0.43	0.60	–	–	0.23	0.14	–	–
Al_2O_3	33.97	34.73	33.81	33.08	29.57	28.95	29.08	29.58	34.56	32.02	34.19	35.12	33.30	32.86	34.59	34.21
Cr_2O_3	0.43	1.16	0.26	0.51	0.83	0.28	0.67	0.77	0.33	0.64	0.78	0.56	0.15	0.94	0.75	0.14
V_2O_3	0.11	–	–	–	–	–	–	0.07	0.08	0.23	0.08	–	0.09	0.25	–	0.10
FeO	0.53	0.57	0.67	0.77	1.52	1.46	1.60	1.39	1.14	1.28	0.53	0.56	0.68	0.48	0.41	0.63
MnO	–	–	–	–	–	–	–	–	–	–	–	–	–	–	–	–
MgO	1.80	1.93	1.89	2.53	3.83	3.88	3.26	3.76	2.13	2.12	1.14	1.82	2.54	1.96	1.28	1.81
CaO	0.33	0.22	0.20	0.28	0.02	0.03	–	0.03	0.05	0.46	0.30	0.13	0.07	0.13	0.17	0.34
Na_2O	0.10	0.13	0.14	0.08	0.17	0.15	0.19	0.16	0.24	0.26	0.22	0.13	0.12	0.15	0.10	0.12
K_2O	4.74	3.80	5.05	4.41	7.53	7.27	7.08	7.62	6.80	6.85	7.05	5.25	6.46	7.31	6.75	6.36
BaO	0.11	–	–	0.14	0.21	0.15	0.18	0.18	–	0.16	–	–	–	0.25	0.18	–
TOTAL	94.60	94.38	94.73	94.35	95.39	96.23	95.06	96.04	94.78	95.29	95.27	94.98	94.97	95.58	95.27	95.67

Structural formulae based on 22 anions

Si	6.73	6.64	6.74	6.75	6.76	6.96	6.92	6.81	6.41	6.62	6.60	6.59	6.64	6.63	6.60	6.65
Ti	–	–	–	–	–	–	–	–	0.04	0.06	–	–	0.02	0.01	–	–
Al(iv)	1.27	1.36	1.26	1.25	1.24	1.04	1.08	1.19	1.59	1.38	1.40	1.41	1.36	1.37	1.40	1.35
Al(vi)	3.81	3.82	3.79	3.71	3.28	3.30	3.34	3.28	3.68	3.48	3.75	3.83	3.66	3.60	3.80	3.76
Al	5.07	5.18	5.05	4.95	4.51	4.34	4.42	4.47	5.26	4.87	5.16	5.25	5.02	4.97	5.21	5.11
Cr	0.04	0.12	0.03	0.05	0.08	0.03	0.07	0.08	0.03	0.07	0.08	0.06	0.02	0.10	0.08	0.01
V	0.01	–	–	–	–	–	–	0.01	0.01	0.02	0.01	–	0.01	0.03	–	0.01
Fe(ii)	0.06	0.06	0.07	0.08	0.16	0.16	0.17	0.15	0.12	0.14	0.06	0.06	0.07	0.05	0.04	0.07
Mn	–	–	–	–	–	–	–	–	–	–	–	–	–	–	–	–
Mg	0.34	0.36	0.36	0.48	0.74	0.74	0.63	0.72	0.41	0.41	0.22	0.34	0.48	0.38	0.24	0.34
Ca	0.04	0.03	0.03	0.04	–	–	–	0.05	–	0.06	0.04	0.02	–	0.02	0.02	0.05
Na	0.03	0.03	0.03	0.02	0.04	0.04	0.05	0.04	0.06	0.06	0.05	0.03	0.03	0.04	0.02	0.03
K	0.77	0.61	0.82	0.72	1.24	1.18	1.17	1.25	1.12	1.13	1.15	0.85	1.05	1.20	1.10	1.03
Ba	0.01	–	–	0.01	0.01	0.01	0.01	0.01	–	0.01	–	–	–	0.01	0.01	–
Total	13.09	13.03	13.13	13.10	13.56	13.45	13.43	13.54	13.48	13.43	13.37	13.20	13.35	13.41	13.31	13.30
Fe/(Fe + Mg)	0.14	0.14	0.16	0.15	0.18	0.17	0.22	0.17	0.23	0.25	0.21	0.15	0.13	0.12	0.15	0.16
X_{Ms}	0.97	0.95	0.96	0.97	0.97	0.97	0.96	0.97	0.95	0.95	0.96	0.96	0.97	0.97	0.98	0.97

– below detection limit.

Table 3
Representative EPMA data of carbonate minerals disseminated in quartz lodes and adjacent wallrocks.

Magnesite–siderite series

CaO	2.41	4.17	3.11	3.51	4.19	5.45	5.09	4.04	5.10	5.11	3.38	–	0.19	–	0.19
MgO	27.16	31.93	33.03	32.84	29.96	22.35	20.01	15.99	14.07	9.57	16.00	10.36	2.17	1.90	1.44
FeO	24.88	17.05	15.75	16.52	18.58	23.33	30.69	33.10	35.74	39.69	32.32	49.62	59.08	61.87	59.71
MnO	0.54	0.16	0.23	0.17	0.12	0.13	0.13	0.06	0.10	0.09	0.31	0.22	0.03	–	0.06
TiO_2	–	–	–	–	–	–	–	–	–	–	–	–	–	–	–
Total	55.01	53.32	52.13	53.04	52.89	51.25	55.91	53.19	55.04	54.45	52.03	60.29	61.47	63.81	61.39

Structural formulae based on a cation per 2 oxygen atoms

Ca	0.04	0.08	0.06	0.07	0.08	0.11	0.09	0.08	0.09	0.09	0.06	–	0.00	–	0.00
Mg	0.49	0.60	0.63	0.62	0.57	0.44	0.36	0.30	0.26	0.18	0.31	0.17	0.04	0.03	0.02
Fe	0.45	0.32	0.30	0.31	0.35	0.46	0.55	0.62	0.65	0.73	0.62	0.82	0.96	0.97	0.97
Mn	0.01	0.00	0.00	0.00	0.00	0.00	0.00	0.00	0.00	0.00	0.01	0.00	0.00	0.00	0.00
Ti	0.00	0.00	0.00	0.00	0.00	0.00	0.00	0.00	0.00	0.00	0.00	0.00	0.00	0.00	0.00

End members

$CaCO_3$	4.38	7.82	5.96	6.62	7.93	10.63	9.10	7.60	9.27	9.37	6.49	0.14	0.30	–	0.30
$MgCO_3$	49.38	59.89	63.37	61.92	56.64	43.60	35.78	30.05	25.57	17.57	30.75	17.19	3.54	2.98	2.34
$FeCO_3$	45.23	31.98	30.21	31.15	35.14	45.52	54.89	62.22	64.94	72.88	62.12	82.30	96.10	96.96	97.26
$MnCO_3$	0.99	0.31	0.43	0.32	0.23	0.25	0.23	0.11	0.19	0.16	0.60	0.37	0.06	0.02	0.10
Sum	99.98	99.99	99.98	100.00	99.94	100.00	100.00	99.98	99.96	99.99	99.97	99.99	100.00	99.96	100.00
Mg/Fe	1.09	1.87	2.10	1.99	1.61	0.96	0.65	0.48	0.39	0.24	0.50	0.21	0.04	0.03	0.02

Breunnerite (last five columns: Calcite veinlets in quartz veins)

CaO	3.19	3.45	4.09	3.62	1.44	3.16	3.15	3.09	1.89	2.75	55.24	56.85	59.69	52.25	56.55
MgO	37.58	36.33	35.69	41.96	42.84	38.88	39.14	39.70	40.51	39.21	1.08	2.37	2.39	1.72	2.05
FeO	13.96	14.35	15.01	10.89	12.18	13.28	13.14	12.90	12.48	13.79	2.31	3.12	1.44	4.02	3.11
MnO	0.12	0.13	0.13	0.04	0.19	0.12	0.12	0.12	0.12	0.13	0.12	0.16	0.21	0.18	0.24
TiO_2	0.03	–	–	–	0.08	0.02	–	0.02	–	0.02	–	–	–	–	–
Sum	54.89	54.25	54.91	56.51	56.73	55.46	55.55	55.83	54.99	55.91	58.75	62.50	63.72	58.17	61.95

Structural formulae based on a cation per 2 oxygen atoms

Ca	0.06	0.06	0.07	0.06	0.03	0.06	0.06	0.06	0.03	0.05	0.94	0.91	0.94	0.90	0.91
Mg	0.68	0.67	0.65	0.74	0.76	0.70	0.70	0.71	0.74	0.70	0.02	0.04	0.04	0.03	0.03
Fe	0.25	0.26	0.27	0.19	0.21	0.24	0.24	0.23	0.23	0.25	0.04	0.05	0.02	0.07	0.05
Mn	–	–	–	–	–	–	–	–	–	–	–	–	–	–	–
Ti	–	–	–	–	–	–	–	–	–	–	–	–	–	–	–

End members

$CaCO_3$	5.82	6.36	7.44	6.40	2.54	5.69	5.67	5.54	3.44	4.91	94.03	90.96	93.67	89.82	91.29
$MgCO_3$	68.47	66.96	65.00	74.25	75.52	70.11	70.46	71.11	73.65	70.13	1.84	3.79	3.75	2.96	3.31
$FeCO_3$	25.43	26.45	27.33	19.27	21.47	23.94	23.65	23.10	22.69	24.67	3.93	4.99	2.25	6.91	5.01
$MnCO_3$	0.23	0.23	0.23	0.08	0.33	0.22	0.22	0.22	0.22	0.24	0.20	0.26	0.33	0.31	0.39
Sum	99.94	100.00	100.00	100.00	99.86	99.96	100.00	99.96	100.00	99.96	100.00	100.00	100.00	100.00	100.00
Fe/Mg	0.37	0.39	0.42	0.26	0.28	0.34	0.34	0.32	0.31	0.35	2.14	1.32	0.60	2.33	1.52

– below detection limit.

homogenization temperatures exclude fluid immiscibility as an entrapment mechanism of the investigated fluid inclusions (cf. Ramboz et al., 1982; Touret, 2001). Post-entrapment modifications may also account for the heterogeneous state and the observed variations of the studied inclusions (Crawford and Hollister, 1986; Huizenga and Touret, 1999). Although inclusions clearly showing textures of post-entrapment modification were avoided in measurements, there is microstructural evidence of recrystallization and grain boundary migration of the host quartz. It is therefore suggested that post-entrapment modifications are likely responsible for variations in the fluid inclusion populations in the quartz lodes.

7.4. Sulfur isotope values

Sulfur isotope values of disseminated pyrite and arsenopyrite in quartz veins and adjacent intensely altered wallrocks are shown in Fig. 10. Generally, most of the values fall within a relatively narrow range, suggesting simple metallogenic history of the Barramiya gold deposit. The calculated $\delta^{34}S$ values of H_2S in some sulfides range between −6.6 and 3.2‰ (Table 5) using temperatures of the fluid inclusions and applying the equations proposed by Ohmoto and Rye (1979). The relative homogeneity of the isotopic data likely implies isotopic equilibrium conditions at the scale of the mineralized quartz veins. The relatively narrow range of $\delta^{34}S_{\Sigma s}$

values of the Barramiya fluids indicates that sulfur was derived from a homogeneous source or that different sulfur components were fairly well mixed in the hydrothermal solutions. The calculated $\delta^{34}S$ values of H_2S are slightly below typical magmatic sulfur values. Either a direct magmatic source, slightly depleted in $\delta^{34}S$ (from granitic intrusions) or an indirect magmatic source may be assumed, involving leaching of isotopically lighter sulfur, either from the volcano-sedimentary host rocks or from disseminated ore in the carbonaceous serpentinite. The positive $\delta^{34}S$ values may be attributed to local reduction of the fluid (c.f. Lambert et al., 1984) by fluid-carbonaceous wallrock interaction, or reactions of the hydrothermal fluids with ^{34}S-enriched sulfides in wallrocks (cf. McCuaig and Kerrich, 1998). Whereas, the lightest value (−6.6) may represent a significantly deformed/metamorphosed sulfide grain. In this case, the near zero measurements may refer to the less deformed sulfides.

8. Discussion

8.1. Listvenite–lode association

Listvenitization is commonly attributed to the emplacement of late-orogenic granitic rocks that produced chloride-rich carbonoaqueous fluids (Likhoidov et al., 2007). The elevated contents of As, Sb,

Table 4
Representative EPMA data of chlorite disseminated in quartz lodes from the Barramiya deposit.

SiO_2	26.76	29.38	28.91	28.93	28.44	28.84	27.99	27.78	28.16	27.11
TiO_2	0.15	0.12	–	–	0.21	0.24	0.17	0.21	0.22	0.13
Al_2O_3	18.50	17.63	18.32	18.95	17.68	19.05	17.58	16.15	17.71	17.48
FeO	17.32	18.69	18.02	19.45	20.82	16.68	18.39	18.60	17.95	18.59
MnO	0.41	0.49	0.62	0.76	0.54	0.91	0.42	0.43	0.48	0.48
MgO	24.45	21.37	21.79	19.45	20.07	21.58	22.82	24.79	22.93	24.16
CaO	0.18	0.18	0.12	0.15	0.23	0.15	0.11	0.23	0.14	–
Na_2O	0.20	–	–	0.02	0.05	0.16	0.16	0.12	0.11	–
K_2O	0.08	–	–	–	–	–	0.04	–	0.06	–
Cl	–	–	–	–	–	–	–	–	–	–
F	–	–	–	0.13	–	–	–	–	–	–
Total	87.40	87.24	87.15	87.23	87.39	86.99	87.03	87.69	87.12	87.41
Formula based on 28 anions										
Si	5.42	5.95	5.85	5.89	5.83	5.81	5.71	5.65	5.72	5.52
Ti	0.02	0.02	–	–	0.03	0.04	0.03	0.03	0.03	0.02
Al(iv)	2.58	2.05	2.15	2.11	2.17	2.19	2.29	2.35	2.28	2.48
Al(vi)	1.84	2.16	2.21	2.44	2.11	2.34	1.93	1.52	1.96	1.72
Al	4.42	4.21	4.37	4.55	4.27	4.52	4.22	3.87	4.24	4.20
Fe(ii)	2.93	3.17	3.05	3.31	3.57	2.81	3.13	3.16	3.05	3.17
Mn	0.07	0.08	0.11	0.13	0.09	0.16	0.07	0.07	0.08	0.08
Mg	7.39	6.45	6.57	5.91	6.14	6.48	6.93	7.52	6.94	7.34
Ca	0.04	0.04	0.03	0.03	0.05	0.03	0.02	0.05	0.03	–
Na	0.08	–	–	0.01	0.02	0.06	0.06	0.05	0.04	–
K	0.02	–	–	–	–	–	0.01	–	0.02	–
Cl	–	–	–	–	–	–	–	–	–	–
F	–	–	–	0.09	–	–	–	–	–	–
Total	20.39	19.93	19.97	19.84	20.01	19.92	20.19	20.41	20.16	20.36
Fe/(Fe + Mg)	0.28	0.33	0.32	0.36	0.37	0.30	0.31	0.30	0.31	0.30

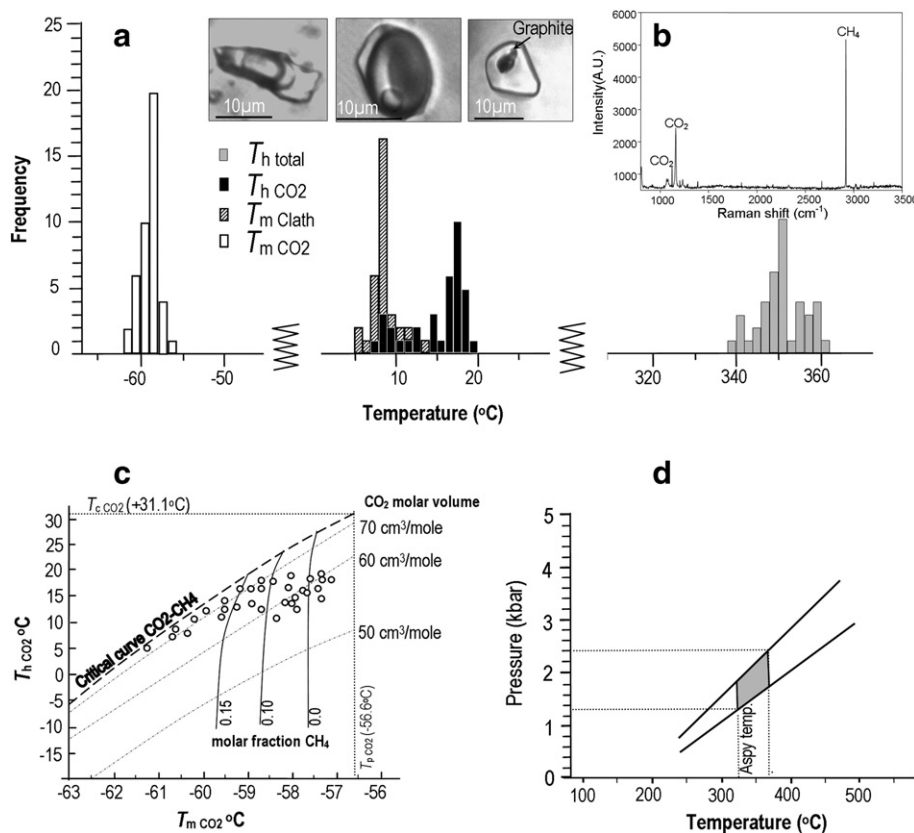– below detection limit.

Fig. 9. (a) Microthermometric data of the aqueous-carbonic inclusions, (b) Raman spectra of CO_2 and CH_4, (c) Homogenization ($T_{h\ CO2}$) vs. melting temperature ($T_{m\ CO2}$) of CO_2 in the investigated H_2O–NaCl–CO_2–CH_4 inclusions (Thiéry et al., 1994). $T_p\ CO_2$ and $T_c\ CO_2$ are triple point and critical temperature of pure CO_2, respectively, (d) P–T field based on isochores for aqueous-carbonic inclusions assuming a H_2O–CO_2–NaCl–CH_4 system (Bakker, 1997).
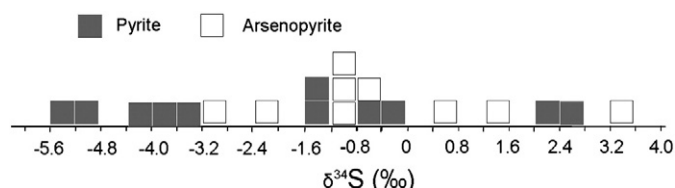
Fig. 10. Histogram showing $\delta^{34}S$ values of disseminated pyrite and arsenopyrite in mineralized quartz veins from the Barramiya deposit.

Table 5
Measured $\delta^{34}S$ (‰) values of sulfides intimately associated with gold and calculated $\delta^{34}SH_2S$ (‰) of the ore fluid.

Sample no.	Mineral	Measured $\delta^{34}S$ (‰)	T (°C)	$\delta^{34}SH_2S$ fluid (‰)
B2	Pyrite	−3.2	340	−4.3
B3	Pyrite	−5.5	335	−6.6
B27	Pyrite	−4.3	340	−5.4
B21	Pyrite	−5.0	330	−6.1
B33	Pyrite	−4.0	365	−5.0
B34	Pyrite	2.6	340	1.5
B26	Pyrite	2.1	360	1.1
B29	Pyrite	−1.5	325	−2.6
B26	Pyrite	−1.5	360	−2.5
B35	Pyrite	−0.7	320	−1.8
B23	Pyrite	−0.3	320	−1.5
B27	Arsenopyrite	3.2	340	2.1
B31	Arsenopyrite	−2.3	320	−3.4
B21	Arsenopyrite	1.0	330	−0.1
B33	Arsenopyrite	−2.9	365	−3.9
B33	Arsenopyrite	1.4	365	0.4
B34	Arsenopyrite	0.5	340	−0.6
B26	Arsenopyrite	−0.6	360	−1.6
B29	Arsenopyrite	−1.0	325	−2.1
B26	Arsenopyrite	−0.8	360	−1.8

Error range related to the analytical uncertainties is ± 0.2. Calculated $\delta^{34}SH_2S$ fluid (‰) is based on differentiation equations of Ohmoto and Rye (1979).
T (°C): temperatures derived from total homogenization of aqueous-carbonic fluid inclusion.

and Hg in listvenites suggest the contribution of granite-related hydrothermal fluids, whereas the presence of Cr, Ni, Co, and Pt point to the ultramafic protolith (see Likhoidov et al., 2007). The present work attests the spatial association of gold-bearing quartz veins and listvenite along a transecting network of steeply dipping faults, shear zones and fractures adjacent to a granodiorite body in the Barramiya mine area. Gold occurs as sub-microscopic mosses, flakes, and blebs (micro-nuggets) in listvenite from the Barramiya mine area (Osman, 2001). Electron microprobe analyses of disseminated Ni-sulfides and Ni-arsenides and pentlandite revealed traces of Au (up to 0.64 wt.%; Takla and Suror, 1996). Accordingly, it is suggested that the serpentinized ultramafic rocks may have been an important source for gold (Takla and Suror, 1996).

8.2. Structural controls on the Barramiya gold deposit

The gold-bearing quartz (± carbonate) veins are spatially and temporally linked to a dextral shear system developed in the late stages of the deformation history of the area. The mixture of massive to heavily deformed microstructures and dynamic recrystallization and slip on discrete carbonaceous laminae in the mineralized quartz veins point to vein formation under variable compressional and tensional regimes (cf. Cox et al., 1987).

Structural readings, including fault planes, slip lineation slickenlines along the vein walls and striations have been collectively used to analyze the paleostress regime prevailing during fault development and vein formation at the Barramiya mine (Fig. 11). Transpression

along the thrust planes and related shear zones (subsequent to F_2 or likely coeval with the F_3 folding event) occurred when the paleostress field was oriented in such a way that σ1 was in the NNW–SSE direction, σ2 was nearly perpendicular to the paleosurface and σ3 was in the ENE–WSW direction (Fig. 11). Limited dip-slip movement along the thrust and shear planes due to density differentiation and sagging down of the heavy ultramafic rocks rotated the paleostress field so that σ1 was oriented normal to the paleosurface. This cyclic conversion from differential to normal stress was concomitant with the dextral transpression along the thrust planes and led to development of discrete shear zones. Dextral transpression continued and gravitational slipping to north was sporadic during the course of quartz veins formation.

8.3. Possible contribution from the granitoid intrusion

The granodiorite dike-like body adjacent to the orebodies is exposed along the host shear/fault system in the mine area. The occurrence as dyke-like body with bifurcated ends suggests that the granodiorite body was likely emplaced at the onset of fault/shear zone development. It is assumed therefore as the heat and fluid source for listvenitization, sericitization and mineralization. The competency contrast between the granitic body and the mélange matrix and serpentinite rocks could lead to the development of an extensive fracture pattern in the intrusion and dilation loci for quartz veins.

Based on the relatively narrow range of $\delta^{34}S_{\Sigma s}$ values of the ore fluids, the homogeneous source of sulfur could have been of direct magmatic origin (the granodiorite intrusion?) or from fairly well-mixed different sulfur components. The mixed sulfur components may be understood in a model of a sulfur-bearing dilute aqueous-carbonic fluid of magmatic origin which leached isotopically light sulfur (plus precious metals) from the listvenized serpentinite on percolation in the shear zone.

8.4. Paragenesis and fluid evolution

Although a simple metallogenic history is inferred, replacement and intergrowth textures in the Barramiya gold deposit indicate an early arsenopyrite + pyrite + pyrrhotite ± gersdorffite assemblage replaced by chalcopyrite, tetrahedrite, sphalerite and galena in a late mineralization stage. Gold occurs both lattice-bound (refractory) and visible, typical of orogenic gold deposits (e.g., Goldfarb et al., 2001; Kolb et al., 2005). Refractory gold is confined to the early assemblage, particularly arsenopyrite and As-pyrite, whereas, minute free-milling gold grains occur as dispersed blebs and specks along the wallrock selvages, and in graphitic shear planes in the quartz veins.

The fluid inclusion study indicates that the ore fluids were low-salinity aqueous-carbonic. Contamination of CO_2-bearing fluids by reaction with rocks containing carbonaceous matter is widely invoked to explain the presence of CH_4 and N_2 in fluid inclusions from shear zone-hosted gold deposits (e.g., Naden and Shepherd, 1989; Shepherd et al., 1991). Hydrolysis of the carbonaceous wallrocks could have enriched the ore fluid in CH_4 and provided the requisite CO_2 for carbonatization. The addition of CH_4 during fluid–rock carbon interaction and carbonate precipitation likely have caused a sharp decrease in fO_2 of the fluid and consequently destabilized gold–sulfur complexes, with sulfur consumption by sulfidation triggering gold deposition. Refractory gold in early sulfide assemblage was deposited from a low-salinity $CO_2 \pm CH_4$–H_2O–NaCl fluid concomitant with the arsenopyrite + pyrite + pyrrhotite ± gersdorffite assemblage, whereas, the free-milling gold could have been mobilized and redistributed during deformation.
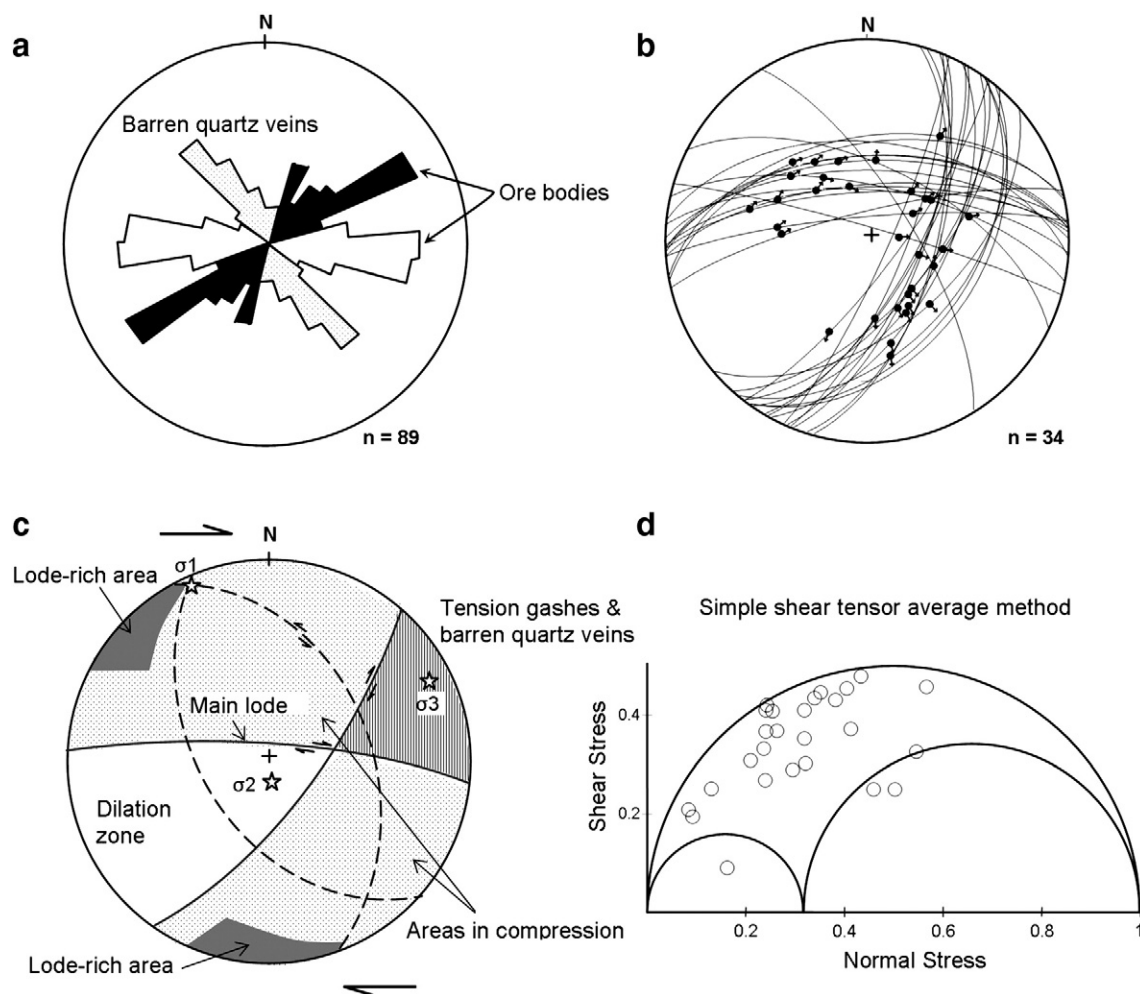
Fig. 11. (a) Rose diagram showing the major fault trends and related quartz veins at the Barramiya mine area, (b) Equal area stereogram (lower hemisphere) of fault planes great circles and slip lineation, slickenlines along the vein walls, (c) Strain directions (principal orthogonal stresses σ1, σ2 and σ3) graphically determined according to the *P* and *T* dihedra method of Angelier and Goguel (1979), and a paleostress tensor comparatively calculated using the inversion algorithm developed by Etchecopar et al. (1981), and interpretation of the right-lateral shear system in relation to the mineralized and barren quartz veins, (d) Mohr diagram showing a distinct high differential stress regime during vein formation.

9. Concluding remarks

The geologic characteristics of the Barramiya deposit; its structural control, host rocks, alteration mineralogy, mineralization style, timing of the mineralization with respect to the deformation history, along with the fluid and stable isotope data, are in accordance with the orogenic mesothermal lode-gold deposit style in the sense of Groves et al. (2003), analogous to other deposits in the Eastern Desert (e.g., Helmy et al., 2004; Zoheir, 2008). The ore fluid characteristics and estimated pressure–temperature conditions of the Barramiya deposit are comparable to other orogenic gold deposits elsewhere in the Eastern Desert (see El-Tokhi and El-Muslem, 2002; Harraz, 2000, 2002; Zoheir, 2008), implying a regional system of greenstone-hosted lode-type gold formations as an integral part of a regional-scale event during the evolution of the Neoproterozoic Arabian–Nubian Shield. However, interplay of a major right-lateral shear system, concurrent(?) emplacement of granodiorite shoot and attendant listvenitization of the ultramafic rocks define a unique scenario of gold mineralization for the Barramiya gold deposit.

References

Anderson, M.R., Rankin, A.H., Spiro, B., 1992. Fluid mixing in the generation of mesothermal gold mineralization in the Transvaal sequence, Transvaal, South Africa. European Journal of Mineralogy 4, 933–948.
Angelier, J., Goguel, J., 1979. Sur une méthode simple de détermination des contraintes pour une population de failles. Comptes Rendus Hebdomadaires des Seances de l'Academie des Sciences 288, 307–310.
Bailey, S.W., 1984. Crystal chemistry of the true micas. In: Bailey, S.W. (Ed.), Micas: Mineralogical Society of America, Reviews in Mineralogy, 13, pp. 13–60.
Bakker, R.J., 1997. Clathrates: computer programs to calculate fluid inclusion V–X properties using clathrate melting temperatures. Computers and Geosciences 23, 1–18.
Botros, N.Sh., 1993. New prospects for gold mineralization in Egypt. Annals. Geological Survey of Egypt 19, 47–56.
Botros, N.Sh., 2004. A new classification of the gold deposits of Egypt. Ore Geology Reviews 25, 1–37.
Bowers, T.S., Helgeson, H.C., 1983. Calculation of the thermodynamic and geochemical consequences of nonideal mixing in the system H_2O–CO_2–$NaCl$ on phase relations in geologic systems: equation of state for H_2O–CO_2–$NaCl$ fluids at high pressures and temperatures. Geochimica et Cosmochimica Acta 47, 1247–1275.

Brown, P.E., 1989. FLINCOR: a microcomputer program for the reduction and investigation of fluid inclusion data. American Mineralogist 74, 1390–1393.

Buckley, H.A., Woolley, A.R., 1990. Carbonates of the magnesite–siderite series from four carbonatite complexes. Mineralogical Magazine 54, 413–418.

Buisson, G., Leblanc, M., 1986. Gold bearing listwaenites (carbonatized ultramafic rocks) in ophiolite complexes. In: Gallagher, M.J., Ixer, R.A., Neary, C.R., Prichard, H.M. (Eds.), Metallogeny of Basic and Ultrabasic Rocks. The Institution of Mining and Metallurgy, London, pp. 121–132.

Collins, P.L.P., 1979. Gas hydrates in CO_2-bearing fluid inclusions and the use of freezing data for estimation of salinity. Economic Geology 74, 1435–1444.

Cox, S.F., Etheridge, M.A., Wall, V.J., 1987. The role of fluids in syntectonic mass transport, and the localization of metamorphic vein-type ore deposits. Ore Geology Reviews 2, 65–86.

Crawford, M.L., Hollister, L.S., 1986. Metamorphic fluids: the evidence from fluid inclusions. In: Walther, J.V., Wood, B.J. (Eds.), Fluid Rock Interaction During Metamorphism. Physical Geochemistry, vol. 5. Springer, Berlin–Heidelberg–New York, pp. 1–35.

Deer, W.A., Howie, R.A., Zussman, J., 1962. Rock Forming Minerals: Sheet silicates, 3. Longman, London. 270 pp.

Diamond, L., 2001. Review of the systematics of CO_2–H_2O fluid inclusions. Lithos 55, 69–99.

Dugdale, A.L., Hagemann, S.G., 2001. The Bronzewing lode-gold deposit, Western Australia: P–T–X evidence for fluid immiscibility caused by cyclic decompression in gold-bearing quartz-veins. Chemical Geology 173, 59–90.

EGSMA, 1992. Geological map of Wadi El Barramiyah Quadrangle, Egypt, scale 1:250, 000. Geological Survey of Egypt.

El-Dougdoug, A., 1990. Gold anomalies in the Late Proterozoic felsic/mafic volcanose-dimentary sequence and associated rocks, Gebel Abu Marawat area, Eastern Desert, Egypt. Bulletin of the Faculty of Science, Cairo University 58, 533–548.

El-Mezayen, A.M., Hassaan, M.M., El-Hadad, M., Hassanein, M.M., 1995. Petrography, geochemistry and ore microscopy of Abu Marawat metavolcanics and associated gold mineralisation, North Eastern Desert, Egypt. Bulletin of the Faculty of Science, Al-Azhar Univeristy 6 (2), 1999–2021.

El-Shazly, E.M., 1977. In: Nairn, A.E.M., Kanes, W.H., Stehli, F.G. (Eds.), Geology of the Egyptian Region. : The Ocean Basins and Margins, vol. 4A. Plenum Press, New York, pp. 379–444.

El-Tokhi, M., El-Muslem, A., 2002. Fluid inclusions in the gold-bearing quartz veins at Um Rus area, Eastern Desert, Egypt. Chinese Journal of Geochemistry 21, 131–139.

Etchecopar, A., Vasseur, G., Daignieres, M., 1981. An inverse problem in microtectonics for the determination of stress tensors from fault striation analysis. Journal of Structural Geology 3, 51–65.

Fonarev, V.I., Touret, J.L.R., Kotelnikova, Z.A., 1998. Fluid inclusions in rocks from the Central Kola granulite area (Baltic Shield). European Journal of Mineralogy 10, 1118–1120.

Gabra, S.Z., 1986. Gold in Egypt. A commodity package: minerals, petroleum and groundwater assessment program. USAID project 363-0105, Geological Survey of Egypt. 86 pp.

Goldfarb, R.J., Groves, D.I., Gardoll, S., 2001. Orogenic gold and geologic time: a global synthesis. Ore Geology Reviews 18, 1–75.

Groves, D.I., Goldfarb, R.J., Robert, F., Hart, C.J.R., 2003. Gold deposits in metamorphic belts: overview of current understanding, outstanding problems, future research, and exploration significance. Economic Geology 98, 1–29.

Halls, C., Zhao, R., 1995. Listvenite and related rocks: perspectives on terminology and mineralogy with reference to an occurrence at Cregganbaun, Co. Mayo, Republic of Ireland. Mineralium Deposita 30, 303–313.

Harraz, H.Z., 2000. A genetic model for a mesothermal Au deposit: evidence from fluid inclusions and stable isotopic studies at El-Sid Gold Mine, Eastern Desert. Journal of African Earth Science 30, 267–282.

Harraz, H.Z., 2002. Fluid inclusions in the mesothermal gold deposit at Atud mine, Eastern Desert, Egypt. Journal of African Earth Sciences 35, 347–363.

Hassaan, M.M., El Mezayen, A.M., Dardir, A.A., Hassanein, M.M., 1996. Primary distribution pattern of gold and associated elements in Abu Marawat mine, North Eastern desert and significance to exploration. Al Azhar Bulletin of Science 7 (1), 995–1016.

Hassaan, M.M., Ramadan, T.M., Abu El Leil, I., Sakr, S.M., 2009. Lithochemical surveys for ore metals in arid region, Central Eastern Desert, Egypt: using Landsat ETM+ imagery. Australian Journal of Basic and Applied Sciences 3, 512–528.

Heinrich, E.W., 1965. Further information on the geology of chromian muscovites. American Mineralogist 50, 758–765.

Helmy, H.M., Kaindl, R., Fritz, H., Loizenbauer, J., 2004. The Sukari Gold Mine, Eastern Desert—Egypt: structural setting, mineralogy and fluid inclusion study. Mineralium Deposita 39, 495–511.

Huizenga, J.M., Touret, J.L.R., 1999. Fluid inclusions in shear zones, the case of the Umwindsi shear zone in the Harare–Shamva–Bindura greenstone belt, NE Zimbabwe. European Journal of Mineralogy 11, 1079–1090.

Klemm, D.D., 1965. Synthesen und Analysen in den Dreieck: diagrammen $FeAsS$–$CoAsS$–$NiAsS$ und FeS_2–CoS_2–NiS_2. Neues Jahrbuch für Mineralogie Abhandlungen 103, 205–255.

Kochine, G.G., Basyuni, F.A., 1968. Mineral resources of the U.A.R., part I, metallic minerals. Internal Report of the Geological Survey of Egypt, 18/1968.

Kolb, J., Rogers, A., Meyer, F.M., 2005. Relative timing of deformation and two-stage gold mineralization at the Hutti Mine, Dharwar Craton, India. Mineralium Deposita 40, 156–174.

Kretschmar, U., Scott, S.D., 1976. Phase relations involving arsenopyrite in the system Fe–As–S and their application. Canadian Mineralogist 14, 364–386.

Kucha, H., Plimer, I.R., Stunpfl, E.F., 1998. Geochemistry and mineralogy of gold and PGE's in mesothermal and epithermal deposits and their bearing on the metal recovery. Fizykochemiczne Problemy Mineralurgii 32, 7–30.

Lambert, I.B., Phillips, G.N., Groves, D.I., 1984. Sulfur isotope compositions and genesis of Archaean gold mineralization, Australia and Zimbabwe. In: Foster, R.P. (Ed.), Gold '82: The Geology, Geochemistry and Genesis of Gold Deposits, Geological Society of Zimbabwe Special Publication 1, pp. 373–387.

Likhoidov, G.G., Plyusnina, L.P., Shcheka, Zh.A., 2007. The behavior of gold during listvenitization: experimental and theoretical simulation. Doklady Earth Sciences 415, 132–734.

McCuaig, T.C., Kerrich, R., 1998. P–T–t–deformation–fluid characteristics of lode gold deposits: evidence from alteration systematics. Ore Geology Reviews 12, 381–453.

Naden, J., Shepherd, T.J., 1989. Role of methane and carbon dioxide in gold deposition. Nature 342, 793–795.

Ohmoto, H., Rye, R.O., 1979. Isotopes of sulfur and carbon. In: Barnes, H.L. (Ed.), Geochemistry of Hydrothermal Ore Deposits. Wiley, New York, pp. 509–567.

Osman, A., 1995. The mode of occurrence of gold-bearing listvenite at El Barramiya gold mine, Eastern desert, Egypt. Middle East Research Centre. Ain Shams University. Earth Sciences Series 9, 93–103.

Osman, A., 2001. The gold metallotect in the Eastern Desert of Egypt. In: Piestrzyhski, et al. (Ed.), Mineral Deposits at the Beginning of the 21st Century, Swets & Zeitinger, Lisse, pp. 795–798.

Ramadan, T.M., 2002. Exploration for gold-bearing listwaenites at Um Khasila area, Central Eastern Desert, Egypt. Egyptian Journal of Remote Sensing and Space Sciences 5, 63–76.

Ramadan, T.M., Sadek, M.F., Abu El Leil, I., Salem, S.M., 2005. Um El Touyur El Fuqani gold mineralization, South Eastern Desert, Egypt: using Landsat ETM+ imagery. Annals of Geological Survey of Egypt 28, 263–281.

Ramboz, C., Pichavant, M., Weisbrod, A., 1982. Fluid immiscibility in natural processes: use and misuse of fluid inclusion data. II. Interpretation of fluid inclusion data in terms of immiscibility. Chemical Geology 37, 29–48.

Sabet, A.H., Bondonosov, V.P., 1984. The gold ore formations in the Eastern Desert of Egypt. Annals. Geological Survey of Egypt 14, 35–42.

Savage, K.S., Bird, D.K., Ashley, R.A., 2000. Legacy of the California gold rush: environmental geochemistry of arsenic in the southern Mother Lode Gold District. International Geology Review 42, 385–415.

Sharp, Z.D., Essene, E.J., Kelly, W.C., 1985. A re-examination of the arsenopyrite geothermometer: pressure considerations and applications to natural assemblages. Canadian Mineralogist 23, 517–534.

Shepherd, T.J., Bottrell, S.H., Miller, M.F., 1991. Fluid inclusion volatiles as an exploration guide to black shale-hosted gold deposits, Dollgelau gold belt, North Wales, UK. Journal of Geochemical Exploration 42, 5–24.

Takla, M.A., Suror, A.A., 1996. On the occurrence of Ni-sulphides and arsenides in some Egyptian serpentinites. Egyptian Mineralogist 8, 1–18.

Thiéry, R., Van den Kerkhof, A.M., Dubessy, J., 1994. V–X properties of CH_4–CO_2 and CO_2–N_2 fluid inclusions: modeling for $T<31$ °C and $P<400$ bars. European Journal of Mineralogy 6, 753–771.

Touret, J.L.R., 2001. Fluids in metamorphic rocks. Lithos 55, 1–25.

Uçurum, A., 2000. Listwaenites in Turkey: perspectives on formation and precious metal concentration with reference to occurrences in East-Central Anatolia. Ofioliti 25, 15–29.

Van den Kerkhof, A.M., Thiéry, R., 2001. Carbonic inclusions. Lithos 55, 49–68.

Zoheir, B.A., 2008. Structural controls, temperature–pressure conditions and fluid evolution of orogenic gold mineralisation in Egypt: a case study from the Betam gold mine, south Eastern Desert. Mineralium Deposita 43, 79–95.